Supporting Information for

Multistable structures inspired by curved-crease origami with pseudo-crease formation

Kevin T. Liu, Tomohiro Tachi and Glaucio H. Paulino

Glaucio H. Paulino.
E-mail: gpaulino@princeton.edu

This PDF file includes:

Other supporting materials for this manuscript include the following:

Movies S1 to S5
Datasets S1 to S3

Supporting Information Text

1. Differential geometry of developable surfaces

In the limit of a thin shell with vanishing thickness, the resistance to bending becomes negligible compared to that of stretching, which causes the shells to behave effectively as inextensible, assuming appropriate loading and boundary conditions. These surfaces can be mathematically modeled as developable surfaces, or surfaces with zero Gaussian curvature. Developable surfaces are a subset of ruled surfaces, which consist of continuous one-parameter family of lines. Equivalently, for any point on a ruled surface, a line can be drawn which lies within the surface. Note that not all ruled surfaces are developable, for instance, the hyperbolic paraboloid.

A ruled surface can be defined by a one-parameter family of lines by

$$\mathbf{S}(u,v) = \mathbf{X}(u) + v\mathbf{R}(u), \tag{1}$$

for $u \in U = [0, u_{\max}]$ and $v \in \mathbb{R}$. The space curve $\mathbf{X}(u) : U \to \mathbb{R}^3$ is known as the directrix, while the unit direction vectors $\mathbf{R}(u) : T \to S^2$ are the ruling directions at different points on the directrix (1). An example ruled surface is shown in Fig. S1A.

For a ruled surface to be developable, the Gaussian curvature must be 0 at all points, and it can be shown that a necessary and sufficient condition is for all $u \in U$,

$$\det(\mathbf{R}(u), \mathbf{R}'(u), \mathbf{X}'(u)) = 0. \tag{2}$$

We can also describe the ruled surface with five scalar functions $K(u), \tau(u), s(u), \varphi(u)$, and $\theta(u)$. The first three functions are the curvature, torsion, and arc-length of the directrix space curve, which have been described classically through the Frenet-Serret formulas:

$$\begin{pmatrix} \mathbf{X}'(u) \\ \mathbf{T}'(u) \\ \mathbf{N}'(u) \\ \mathbf{B}'(u) \end{pmatrix} = s'(u) \begin{pmatrix} 1 & 0 & 0 \\ 0 & K(u) & 0 \\ -K(u) & 0 & \tau(u) \\ 0 & -\tau(u) & 0 \end{pmatrix} \begin{pmatrix} \mathbf{T}(u) \\ \mathbf{N}(u) \\ \mathbf{B}(u) \end{pmatrix}, \tag{3}$$

where the tangent, normal, and binormal vectors $(\mathbf{T}(u), \mathbf{N}(u), \mathbf{B}(u))$ form an orthonormal frame. The last two functions are the inclination angle $\varphi(u) : [0, u_{\max}] \to (-\pi, \pi]$ and the ruling angle $\theta(u) : [0, u_{\max}] \to (0, \pi)$. The inclination angle $\varphi(u)$ is the signed angle between the osculating plane of the directrix with normal direction $\mathbf{B}(u)$ and the tangent plane $\Pi(u)$ of the surface with normal direction $\mathbf{P}(u)$ such that

$$\mathbf{P}(u) = \cos\varphi(u)\mathbf{B}(u) + \sin\varphi(u)\mathbf{N}(u). \tag{4}$$

The ruling angle $\theta(u)$ defines the rule lines as

$$\mathbf{R}(u) = \cos\theta(u)\mathbf{T}(u) + \sin\theta(u)(\mathbf{P}(u) \times \mathbf{T}(u)) \tag{5}$$

$$= \cos\theta(u)\mathbf{T}(u) + \sin\theta(u)(\cos\varphi(u)\mathbf{N}(u) - \sin\varphi(u)\mathbf{B}(u)), \tag{6}$$

which lies in the tangent plane $\Pi(u)$. The Frenet-Serret frame, inclination angle, ruling angle, and surface normal direction are indicated in Fig. S1A.

The developability condition [2] can be expressed in terms of the five scalar functions as

$$K(u)\sin\varphi(u)\cot\theta(u) = -\tau(u) + \frac{\varphi'(u)}{s'(u)}. \tag{7}$$

Now, suppose that we are given a space curve $\mathbf{X}(u)$ as a directrix with curvature $K(u)$, torsion $\tau(u)$, and parametrization speed $s'(u)$, and a developed patch with a defined boundary curve $\mathbf{x}(u)$ with signed curvature $k(u)$ and the same parametrization speed $s'(u)$, as in Fig. S1B. We are asked to solve for the shape that results from bending the flat patch such that the boundary curve matches the directrix. The three scalars related to the directrix are constrained by the given space curve. Using the constraint for developability, the inclination angle $\varphi(u)$ and the ruling angle $\theta(u)$ can be solved. If $|K(u)| > |k(u)|$, the inclination angle is found to be

$$\varphi(u) = \pm\arccos\frac{k(u)}{K(u)}. \tag{8}$$

Note that $k(u)$ will match the geodesic curvature of $\mathbf{X}(u)$ on the ruled surface, as geodesic curvature is an intrinsic quantity. The ruling angle is found to follow

$$\cot\theta(u) = -\frac{\tau - \frac{\varphi'(u)}{s'(u)}}{K(u)\sin\varphi(u)}. \tag{9}$$

If $k(u) \neq 0$, there are two possible values of inclination angle, which in general results in different surfaces. From this result, there are only a finite number (in general, 2) of configurations of a given surface glued to a given space curve that requires no

stretching. Any other configuration, including intermediate states between these configurations are non-isometric and require energy for stretching.

In the case of curved origami, in which a single planar sheet is folded along a curved crease, the development of the shared boundary is identical for each patch on either side of the boundary. If the bent configuration of one patch is fixed, the crease line also becomes a fixed space curve. Therefore, from the previous result, the free patch only has in general two stretch-free configurations.

In addition, in the case of curved origami, from [8] one can show that the inclination angle of the patch on the left must have the same magnitude as on the right, i.e., $\varphi_L(u) = \pm\varphi_R(u)$. If $\varphi_L(u) = \varphi_R(u)$, the fold angle of the crease is zero. If $\varphi_L(u) = -\varphi_R(u)$, the folded shape can be found by solving an initial value problem.

For the special case of a planar creases, $\tau(u) = 0$, and one can show that $\theta_L = \theta_R$, meaning that the rule lines in the development are continuous through the crease. In this case, the two stretch-free configurations correspond to one where $\varphi_L(u) = \varphi_R(u)$ and the crease remains unfolded, and one where $\varphi_L(u) = -\varphi_R(u)$ and the free surface is the reflection of the first configuration about the crease plane. For more discussion on non-planar creases, see SI Appendix, section 11.

2. Finite Element Modeling

The numerical modeling was conducted using ABAQUS implicit dynamic analysis. For simplicity, we assumed that the folding stiffness from the crease is negligible, and therefore only modeled the central free surface. We also assumed that the deformation is symmetric about the yz-plane. The nodes on the bottom crease had their displacement fixed but were free to rotate. The nodes on the top crease were pinned to a rigid body representing the rigid top surface. The material model was chosen to be elastic for simplicity, with $E = 1030$ MPa (from polypropylene tensile tests) and $\nu = 0.45$ (from literature (2)).

Two sets of simulations were conducted. First, a pure bending simulation was conducted, as shown in Fig. 1. Next, loading test simulations to reflect the experimental setup shown in Fig. 5 were conducted. We will briefly describe these numerical simulations.

For the pure bending simulation, the surface is initially cylindrical. A symmetry boundary condition is applied along the xy plane. First a modal analysis is conducted to find the 4 lowest eigenmodes of the shell. These are normalized by their maximum displacement, summed, and scaled by $\frac{\epsilon}{4}$ and applied as an imperfection to the model, where $\epsilon = 0.2$ mm is a small imperfection magnitude. The addition of the imperfection causes the creases to snap asymmetrically, which is observed in the physical models. A pinned boundary condition is applied to the bottom crease nodes, which fixes their displacement but allows rotation. Next, to model the rigidity of the top handle, a pinned rigid body constraint was applied to the crease edges, which allowed rotation at the crease nodes but prevented relative displacement. Then a rotational displacement boundary condition is applied to the upper handle rigid body.

The loading conditions we applied in the simulation were informed by interacting with physical prototypes. Loading conditions were designed to explore all the deformation branches that we found in the physical prototypes. In some simulations, for instance, sequence 2 in SI Video 2, the rotation is paused at specified angles, and a small horizontal point force is applied to the top rigid body reference point in order to transition the structure to a new deformation branch. This allows us to explore a different branch that would not be accessible from rotation alone. Specific details on loading conditions are discussed in Section 4. We were able to replicate all the deformation branches that we observed in the physical prototypes, however, it is possible that other stable deformation branches exist.

For the loading test simulations, we model the bending of the shell from an initially flat sheet in order to capture the tendency for the surface to flatten away from the rigid constraints. The modeled shell is initially flat, and a displacement is applied in the z for the crease nodes to curve the crease edge onto a cylindrical surface. The displacement w follows

$$w(x) = -R(\cos(\frac{x}{R}) - 1.0). \quad [10]$$

Next the modal analysis is conducted to find the 6 lowest eigenmodes to apply an imperfection. Rigid body constraints are applied to both the top and bottom creases, with the location of the rigid body reference point at the attachment points of the load-displacement tester. Then the bottom rigid body reference point is pinned, and a displacement control is applied to the top rigid body reference point to simulate the motion of the tester head.

For both models, S8R quadratic shell elements were used to mesh the deformable surface. Quadratic elements were chosen to better model the curved surfaces and creases. In addition, quadratic elements were found to behave more predictably when small imperfections were introduced. The mesh size is approximately 2 mm x 2 mm.

Fig. S2A plots the total strain energy, artificial energy, and kinetic energy against the simulation time of the baseline geometry. We observe that the kinetic and artificial energy are negligible compared to the strain energy, which confirms quasi-static assumption and shows that the stabilization energy is not excessive. Fig. S2B shows the comparison of the branch diagrams between the baseline simulation and a mesh refinement using 1 mm x 1 mm elements. One can see that the results are nearly identical.

3. Pseudo-creases

The intermediate stable states B, B', C, and C' in Fig. 2 have deformation concentrated along bands which roughly lies in a plane containing the ends of one crease and the center of the opposite crease. This suggests that the structure is forming its own "pseudo-crease" which concentrates the deformation in a limited region. We compare the simulated intermediate state with

the shape found by reflecting the surface about one pre-existing crease and one planar crease defined by the points contained by the "pseudo-crease", and find close resemblance, as shown in Fig. S3.

For instance, for stable state C, shown in Fig. S3A, the plane containing the ends of the bottom crease and the middle of the top crease is inclined at an angle $\theta_p = 74.7^\circ$. The angle of the top crease with the horizontal is $\theta = -65^\circ$ (negative because the plane is oriented below the horizontal. Approximating the pseudo-crease as a sharp crease, we can predict the deformed shape by applying reflections about the crease planes.

The surface folds an angle $|\pi - 2\theta_p|$ at the pseudo-crease crease, and folds an angle $|\pi - 2\theta|$ at the top crease. Because each reflection reverses the direction of the rotation, when summing the total angle we alternate the signs. The predicted rotation of the top handle is

$$\phi^* = |180^\circ - 2(74.7^\circ)| - |180^\circ - 2(-65^\circ)| \quad [11]$$
$$= -279.4^\circ = 80.6^\circ. \quad [12]$$

Fig. S3A shows the predicted deformed shape in red superposed on the simulated stable state. The simulated rotation angle of stable state C is 80.4°.

For stable state B, shown in Fig. S3B, the plane containing the ends of the top crease and the middle of the bottom crease is inclined at an angle $\theta_p = -74.7^\circ$. The predicted rotation of the top handle is

$$\phi^* = |180^\circ - 2(-74.7^\circ)| - |180^\circ - 2(65^\circ)| \quad [13]$$
$$= 19.4^\circ. \quad [14]$$

Fig. S3B shows the predicted deformed shape in red superposed on the simulated stable state. The simulated rotation angle of stable state B is 16.2°. Differences in the predicted shape and the simulated shape can be explained by the finite radius of curvature of the pseudo-crease, rather than a sharp crease.

For some geometries, we can find stable states with more than one pseudo-crease. For instance, for parameters ($R = 65$ mm, $s_0 = 30$ mm, $\theta = 50^\circ$, $g = 6$ mm, $t = 0.25$ mm), we find stable states with two pseudo-creases, see Fig. S3C. We find the plane containing the ends of a crease and the center of the shell have $\theta_p = 64.3^\circ$. The predicted rotation of the top handle is

$$\phi^* = |180^\circ - 2(50^\circ)| - |180^\circ - 2(64.3^\circ)| + |180^\circ - 2(-64.3^\circ)| - |180^\circ - 2(-50^\circ)| \quad [15]$$
$$= 57.2^\circ. \quad [16]$$

The simulated rotation angle is 49.4°, which shows a greater difference that the previous stable states, likely because additional pseudo-creases compounds the error of the sharp crease approximation.

4. Branches

Here we qualitatively describe the branches of the state space found in the numerical simulations for two samples, which are shown in Fig. S4. In Fig. S4A, B_0 corresponds to the branch containing the initial state, with both creases unfolded. B_2 corresponds to the branch containing the fully folded state with both creases folded. Qualitatively, both branches exhibit wrinkles in the center of the shell. B_1 and $B_{1'}$ correspond to branches where one crease is folded, and one pseudo-crease. B_1 and $B_{1'}$ are mirror symmetric to each other. To explore these branches, two bending simulations were conducted, as shown in SI Video 2. In the first simulation, the rotation angle ϕ of the top handle was swept from 0° to 5°, back to 0°, 180° and back to 0°. This uncovered the branches (in order) B_0, $B_{1'}$, B_2, and a portion of B_1. In the second simulation, to access the unexplored portion of B_1, a horizontal point force was applied to the handle to transition to branch B_1, at which point the handle was rotated again.

For different geometries, particularly with low thickness and θ angle, we can find new branches in addition to the ones previously discussed. For example, in the sample shown in Fig. S4B with ($R = 65$ mm, $s_0 = 30$ mm, $\theta = 50^\circ$, $g = 6$ mm, $t = 0.25$ mm), Branch B_3 has two pseudo-creases which are off-center, and Branch B_4 have two pseudo-creases which are centered. Branch B_5 has two centered pseudo-creases and two folded creases. Similar to the sample in Fig. S4A, two bending simulations were conducted. In the first simulation, the rotation angle ϕ of the top handle was swept from 0° to 180° and back to 0°. The sample followed branches (in order) B_0, B_3, B_4, and $B_{1'}$. Due to the symmetry of the sample, we knew that a branch corresponding to $B_{1'}$ existed. In addition, we expected from interacting with the physical samples that a branch containing the second isometric configuration existed. Therefore, in a separate simulation we applied a horizontal force to the handle to transition to B_1, rotated the handle from 0° to 180°, applied another horizontal force to transition to branch B_2, and rotated the handle back to 0°. For the second simulation the sample followed B_0, B_1, B_2, B_5, and $B_{1'}$.

A number of snapshots of the simulation at states other than the local energy minima are shown in the insets of Fig. S4. These higher energy states have a greater degree of panel deformation and strain energy.

It should be noted that the total number of creases or pseudo-creases is always even, reflecting the fact that an even number of reflections is required to keep the original top handle unmirrored. We also note that additional stable branches that have not been shown may exist. For instance, it is likely there is an additional branch that is a mirror reflection to B_3 where the pseudo-creases connect to the opposite handle.

5. Varying shell thickness

We varied the shell thickness and applied rotational sweeps from 0 to π to 0 radians, and observed the effect on the mechanical behavior. We conducted simulations for thicknesses of 0.3, 0.4, 0.5, 0.6, and 0.7 mm. Note that 0.5 mm is the thickness used in the baseline model.

Referring to the motion branches shown in Fig. 2 and Fig. S4A, the sequence of branches the baseline model followed was $B_0 \to B_{1'} \to B_2 \to B_1$, or in words, central wrinkles $\to$ one folded crease and one pseudo-crease $\to$ two folded creases $\to$ one folded crease and one pseudo-crease.

Fig. S5 shows the branches followed for the rotation sweeps for the various thicknesses for ($R = 55$ mm, $s_0 = 30$ mm, $\theta = 65^\circ$, $g = 6$ mm)

- 0.3 mm: $B_0 \to B_{1'}$
- 0.4 mm: $B_0 \to B_{1'}$
- 0.5 mm: $B_0 \to B_{1'} \to B_2 \to B_1$
- 0.6 mm: $B_0 \to B_{1'} \to B_2 \to B_1$
- 0.7 mm: $B_0 \to B_{1'} \to B_2 \to B_1$

Qualitatively, the shapes of the branches remain the same for the different thicknesses. We see that for the two thinnest samples, they transition to Branch $B_{1'}$ but do not transition to branch B_2 from rotation alone. Note that the four branches found may not be the only branches that exist, and indeed for different geometries we can detect different branches.

We repeated the simulations for a sample with ($R = 65$ mm, $s_0 = 30$ mm, $\theta = 50^\circ$, $g = 6$ mm) and thicknesses of 0.15 mm, 0.2 mm, 0.25 mm, and 0.3 mm. The motion branches are shown in Fig. S6. We see additional branches exists, highlighted in Fig. S4B. Fig. S6 shows the branches followed for the rotation sweeps for the various thicknesses.

- 0.15 mm: $B_0 \to B_3 \to B_4$
- 0.20 mm: $B_0 \to B_3 \to B_4 \to B_{1'}$
- 0.25 mm: $B_0 \to B_3 \to B_4 \to B_{1'}$
- 0.30 mm: $B_0 \to B_{1'}$
- 0.35 mm: $B_0 \to B_{1'}$

We see that the thinnest two samples in Fig. S5 stay on Branch $B_{1'}$ without transitioning to Branch B_2, the thinnest sample of Fig. S6 stays on Branch B_4 without transitioning to Branch $B_{1'}$. This suggests the lower bending stiffness keeps the branches stable for longer, preventing additional creases from folding. The thickest two samples of Fig. S6 only show branches B_0 and $B_{1'}$, without the existence of states B_3 and B_4 with two pseudo-creases. We theorize the greater thickness makes bending two pseudo-creases unstable.

From shell theory (3), the elastic strain energy density per unit area (U) of a shell element can be separated into stretching (U_S) and bending (U_B) components

$$U_S = \frac{Et}{2(1-\nu^2)}(\varepsilon_x^2 + 2\nu\varepsilon_x\varepsilon_y + \varepsilon_y^2) + \frac{Et}{(1+\nu)}\frac{\gamma_{xy}^2}{4}, \quad [17]$$

$$U_B = \frac{Et^3}{24(1-\nu^2)}(\kappa_x^2 + 2\nu\kappa_x\kappa_y + \kappa_y^2) + \frac{Et^3}{12(1+\nu)}\kappa_{xy}^2, \quad [18]$$

where ε and κ are the strains and curvatures respectively, and E and ν are the elastic modulus and Poisson's ratio respectively. We wish to observe in the numerical simulations how each energy component scales with thickness to gain intuition on how the mechanical behavior varies with thickness. The stretching and bending energy were calculated using [17] and [18] from the strains and curvatures found in simulation. Fig. S7A shows the plots of the stretching and bending energy density for the stable state at $\phi = 18^\circ$ for a shell of thickness 0.5 mm. Fig. S7B shows a plot the respective energies plotted throughout the deformation for a number of shell thicknesses.

We can make a couple qualitative observations. From the deformed shape in Fig. S7A, the bending energy dominates the strain energy along the pseudo-crease, while stretching is concentrated along the outer edges of the bottom crease the center of the top crease.

Next, observing the total energy versus angle plot at the bottom of Fig. S7B, we see that initially, the energy is primarily in-plane, consistent with the expected stress distribution in small deformation beam bending. Then, at the first snap, which occurs at $\phi \approx 8^\circ$, the stretching energy decreases while the bending energy (primarily along the pseudo-crease) increases, causing a net decrease in energy. Further rotation up to $\phi \approx 35^\circ$ increases stretching energy and decreases bending energy. Then from $35^\circ < \phi < 65^\circ$ both energies are approximately constant, as the pseudo-crease plane shifts. As ϕ further increases, the bending energy increases, while the stretching energy decreases before increasing after the second stable state. Then the second snap occurs, where primarily the bending energy is relieved.

For the thin shells, the stretching energy is approximately symmetric about $\theta = 50°$, which is half the angle of rotation to the second stable state. Meanwhile, the bending energy is greater for $\theta > 50°$, due to the initial curvature of the shell in the zero stress state.

Next, we consider how strain energy scales with thickness. Suppose that the stretching, bending, and total energy for a given rotation angle and branch are $E_s(t), E_b(t)$, and $E(t)$ respectively, which are functions of thickness t. In general, for a thin shell, stretching energy scales $\propto t$ and the bending energy scales $\propto t^3$. However, as the thickness of the shell changes the shape of the surface also changes to minimize the total strain energy.

For instance, if the thickness of the surface increased slightly from t_0 to λt_0 for $\lambda > 1$, the surface would tend to allow more stretching to relieve areas of high curvature. As a result,

$$E_s(\lambda t_0) > \lambda E_s(t_0), \quad [19]$$

$$E_b(\lambda t_0) < \lambda^3 E_b(t_0), \quad [20]$$

$$E(\lambda t_0) < \lambda E_s(t_0) + \lambda^3 E_b(t_0). \quad [21]$$

To verify this result, we observe the energy values in the numerical simulation given in Fig. S7C, recreated in Fig. S8, with additional simulated thicknesses. Fig. S8A and S8C plot the stretching and bending energy points respectively. In addition, a cubic polynomial fit is applied. For each stretching energy data point, we plot a small linear section which corresponds to a linear scaling of E_s with t, and for each bending energy data point, we plot a small cubic section which corresponds to a cubic scaling of E_b with t. We can observe from the residual plots in Fig. S8B and Fig S8D that the simulated stretching energies scale faster than linearly, and the bending energies scale slower than cubically, verifying Equations 19 and 20.

Next, in Fig. S8E the total strain energy is plotted with a cubic polynomial fit. For each data point, we plot a small segment which corresponds to the sum of the linear and the cubic scalings, and we see in the residual plot of Fig S8F that the curve is nearly tangent to the simulated total strain energies, with the simulated total energy close to the minimum predicted from scaling and summing, verifying Equation 21.

The tendency for the deformation to concentrate in a narrow band in our samples is analogous to a result shown by Lobovsky et. al. (4) in crumpled thin elastic sheets, where deformation is concentrated to a ridge. They show that that as the stretching moduli G decreases from a very large value the shape of the ridge changes from a sharp crease to a kite like shape. Through order of magnitude scaling arguments, they suggest that for thin shells, bending and stretching energy will have similar orders of magnitudes, and the total energy scales with $\kappa \cdot (\frac{X}{t})^{1/3}$, where κ is the bending stiffness, X is the sample length, and t is the shell thickness. Accordingly, the total energy scales with $t^{8/3}$, which is near the scaling coefficient we see in the simulations shown in Figure S7, though the geometry of our sample is different from that studied by Lobovsky et. al.

Another factor that may contribute to the deviation of the expected scaling laws is the deviation from the thin-shell approximation. Often times in the literature, the thin shell limit involves thickness to shell curvature ratios < 0.01 (3). While our samples have a ratio of $\frac{t}{R}$ on the order of 0.01, the curvature of the shell throughout the deformation, particularly in the pseudo-crease, can become much higher than the initial shell curvature.

6. Variation of parameters

Thus far we have shown the theoretical basis for multistability and demonstrated the ability for numerical simulations to recreate the multistability observed in physical samples. Next, we wish understand how varying geometric parameters affect mechanical behavior in order to be able to achieve desired properties in a design. To this end, we repeat the numerical simulations, varying a single geometric parameter while keeping all others constant and observing the impact on mechanical response such as stiffness, peak moment, and stable states.

Plane inclination angle θ. First, we varied the plane inclination angle θ and performed rotation sweeps, where the handle angle was increased from 0 rad to π rad and back to 0 rad. Fig. S7E shows the moment vs. rotation angle plots for a variety of θ values. Solid lines represent the forward portion, while dotted lines represent the reverse portion. There is an initial high stiffness, before one of the creases snaps at about $\phi = 10°$. Later, in samples with $\theta \geq 65°$, the second crease snaps. We observe that the samples with low θ cannot achieve the second snap from rotation alone. Later experiments also show the general result that the branch where both creases are folded is easier to reach with higher values of θ. We also find that the increasing θ results in lower stiffness and energy barrier, as shown in Fig. S7G. Increasing θ increases the length of the shell at the edges, which decreases the effective stiffness in tension.

Geometry predicts that the second stable state can be found by applying reflections about the two crease planes, which results in a rotation angle of $\phi^* = 2\pi - 4\theta$, which is reflected in the zero crossings shown for the dotted $\theta = 65°, 70°$, and $75°$ curves of Fig. S7E.

Thickness. Next, we found that varying the thickness affects the stability of the branches, though the qualitative nature of the branches are unchanged (see SI Appendix, section 5). This allows a comparison between structures with different thicknesses provided that they are in the same branch. If the deformed geometry remained unchanged while the thickness varies, one would expect $U_S \propto t$ and $U_B \propto t^3$. However, as the thickness varies, the equilibrium geometry varies in order to minimize the total elastic energy. For instance, if the thickness increases, the radius of curvature for a pseudo-crease also increases, relieving some bending energy while increasing the stretching energy.

The highlighted portion of Fig. S7B is a range of rotation angles in which all of the samples simulated had the same deformation branch. Fig. S7C plots the strain energies for a given rotation angle as the shell thickness is varied. We calculated a power law fit to find the scaling coefficients of the energies with respect to shell thickness. We repeated this for the entire range of angles in the highlighted region and plotted the scaling power in Fig. S7D. We see that bending energy increases slower than the $\propto t^3$ rate and stretching energy increases faster than the predicted $\propto t$ rate, with a net effect of total elastic energy scaling slower than the rate expected by scaling the U_S and U_B by t and t^3 respectively and summing. See the SI Appendix, section 5 for more discussion on the scaling rate of the respective energies. In Fig. S7D we can also see that the scaling powers vary with the folding angle, making it difficult to make general statements for how energy scales for different geometries. Lastly, Fig. S7H shows the trend of increasing peak moment as shell thickness increases.

Radius of curvature R and semi-arc length s_0. Next, we wish to vary the radius of curvature and arc length to observe the change in the energy barrier between the two primary stable states. Fig. S7I and J show moment vs. angle plots, varying R or s_0 respectively and keeping all other parameters constant.

As a proxy for sample stiffness and peak moment, we calculate the second moment of inertia of a circular arc. We assume the thickness t is low. The location of the neutral axis is

$$\begin{aligned}\bar{y} &= \frac{1}{2s_0}\int_{-s_0}^{s_0} R(1-\cos(\frac{s}{R}))ds \\ &= R - \frac{R^2}{s_0}\sin(\frac{s_0}{R})\end{aligned}$$

The second moment of inertia is then

$$\begin{aligned}I &= t\int_{-s_0}^{s_0}(R(1-\cos(\frac{s}{R})) - \bar{y})^2 ds \\ &= t\int_{-s_0}^{s_0}(-R\cos(\frac{s}{R}) + \frac{R^2}{s_0}\sin(\frac{s_0}{R}))^2 ds \\ &= tR^2(\frac{R^2}{s_0}\cos(\frac{2s_0}{R}) + \frac{R}{2}\sin(\frac{2s_0}{R}) + s_0 - \frac{R^2}{s_0})\end{aligned}$$

If $R \gg s_0$

$$\begin{aligned}I &\approx t\frac{R^4}{s_0}[1 - \frac{1}{2}(\frac{2s_0}{R})^2 + \frac{1}{24}(\frac{2s_0}{R})^4 - \frac{1}{720}(\frac{2s_0}{R})^6 + \ldots] + \ldots \\ &\quad + t\frac{R^3}{2}[(\frac{2s_0}{R}) - \frac{1}{6}(\frac{2s_0}{R})^3 + \frac{1}{120}(\frac{2s_0}{R})^5 + \ldots] + ts_0R^2 - t\frac{R^4}{s_0} \\ &\approx t\frac{R^4}{s_0}(\frac{2}{3}(\frac{s_0}{R})^4 - \frac{4}{45}(\frac{s_0}{R})^6) + t\frac{R^3}{2}(-\frac{4}{3}(\frac{s_0}{R})^3 + \frac{4}{15}(\frac{s_0}{R})^5) + O((\frac{s_0}{R})^7) \\ &\approx \frac{2}{45}\frac{s_0^5}{R^2} + O((\frac{s_0}{R})^7)\end{aligned}$$

Therefore, we should expect that decreasing R and increasing s_0 should result in greater stiffness and energy barrier. However, the nature of the deformation is complex, involving nonlinearity and instability. Varying R and s_0 affect factors other than I that affect the energy barrier, such as the length of the shell at the edges of the sample. Fig. S7I and J show that power laws fit the peak moment very well for the given geometries, though with slightly different exponents from those predicted from the second moment of inertia alone.

To further explore the influence of the radius of curvature and arc length, we conducted simulations to find the peak moment for geometries varying R and s_0 simultaneously, shown in Fig. S9. Beginning with a reference geometry presented in Fig. S4A, we scaled the radius of curvature from 80% to 130% of the original 55 mm, and scaled the semi-arc length from 80% to 120% of the original 30 mm, while keeping other parameters constant. There were 30 combinations of (R, s_0) simulated, shown in Fig. S9A. For each simulation, we show a sketch of the sample cross section in red and a sketch of the moment versus rotation profile in green. The moment versus rotation profiles show rotations from 0° to 15°. In Fig. S9B, the peak load for each simulation is shown, with contours showing the interpolation of peak moments. As expected, low R values and high s_0 result in greater peak loads. Similar design maps could be created for different geometric parameters and for other geometries of interest.

Gap g. Lastly, we varied the gap length and plotted the peak moment in Fig. S7K. Unlike the other geometric parameters, which primarily affect the mechanics of each crease independently, the gap length affects the level of interaction between the two creases. This causes a highly non-linear relationship between the peak moment and g.

At one extreme, as g approaches 0, there is little material at the center of the sample to compress. Thought of in terms of beam bending, the neutral axis shifts towards the center, and the outer edges must stretch significantly as the sample bends, resulting in high peak moment. At the other extreme, the sample resembles a long tape spring. The deformation is localized to a central portion of the shell, and the peak moment is independent of the total length and therefore approaches a constant

value. Between these two extremes, we find that the peak moment does not decrease monotonically; instead, there is a range of g near 7 mm in which the peak moment plateaus. We theorize in this region the deformation prior to the snap is localized near one of the creases, resulting in weak dependence on the length of the sample. Deformed shapes from simulations to support this theory are shown in SI Appendix, section 7.

7. Relationship between gap length g and peak moment

The gap length g affects the level of interaction between the two creases. This causes a highly non-linear relationship between the peak moment and g. Fig. S10A recreates the plot shown in Fig. 4G, with additional data points. In addition, Fig. S10B show snapshots of the shells colored by energy density at the moment they exert their peak moment for five specific thicknesses.

Based on the strain energy distribution, we theorize a mechanistic explanation for the relationship between the peak moment and gap length. At very low values of g, there is little material at the center of the sample to compress, causing the neutral axis to shift inwards and the second moment of inertia to increase. For intermediate values of g, such as $g = 5$ mm, 6.25 mm, and 8mm, the deformation is localized near one crease, resulting in a relatively weak relationship between peak moment and g. For large values of g, the deformation is localized in the center of the shell, resembling a tape spring in bending, so the peak moment approaches a constant value.

8. Experimental Validation

Fig. S11 shows the experimental setup designed to test the multistable samples along with a free body diagram. We replicated this setup in numerical models, as described in section 2.

We tested and simulated for 6 sample geometries, such that all geometric parameters were varied. In the given test setup, inclination angles below $\approx 65^\circ$ would result in collisions before the full range of deformation was tested, as seen in Fig. S12A. In addition, high inclinations approaching 90° would result in very long creases which are difficult to physically realize, as seen in S12B. As a result, the inclination angles used were 70° and 75°.

The simulated results are overlaid on experimental results in Fig. S13. We find good correspondence visually between the deformation sequence. Arrows between plots indicate where samples differ only by one geometric parameter, isolating its impact on the mechanical behavior.

The simulations and experiments have good agreement, confirming the trends predicted by simulations, in which increasing shell thickness results in higher stiffness, decreasing θ results in higher equilibrium fold angle and higher peak load, lowering g results in earlier snapping, and lowering R and increasing s_0 results in higher peak load.

However, there are some differences between simulations and experiments. The experiments show a significant jump in the load at each snap, while the simulations tend to have a more gradual decrease in load. Additionally, the initial stiffness of the simulations tends to be greater than that of the sample. For simplicity, various details were not modeled in the simulations which can explain differences with the experiments. The simulations do not model the crease stiffness, while the samples are pre-creased, in which the material at the crease are plastically deformed, which acts to make the snap more dramatic. Rather than elastic, the polypropylene sheet is a viscoelastic material, which causes a rate dependence on the load profile. In addition, from 3D scans of the physical samples (see section 9), the physical samples tend to "flatten" more than the simulations predict, which could explains the lower initial stiffness than that predicted in the simulated elastic model.

9. 3D scans of samples

We conducted 3D scans of samples in their initial state using an Einscan-SP tabletop scanner (5). Fig. S14 shows a comparison between the the scanned shape and the simulated shape from bending a flat sheet as described previously for a samples with parameters ($R = 55$ mm, $s_0 = 30$ mm, $\theta = 60^\circ$, $g = 9$ mm, $t = 0.5$ mm) and ($R = 75$ mm, $s_0 = 30$ mm, $\theta = 75^\circ$, $g = 6$ mm, $t = 0.5$ mm). We found good agreement between the simulation and scan for the sample with $R = 55$ mm, however the simulation underestimates the flattening effect for the sample with $R = 75$ mm. Exploring what factors impact the rate of flattening requires further study.

10. Bench preliminary design

Designing load-bearing multistable origami structures on the architectural scale poses several challenges, such as crease design. Another primary challenge is designing a structure that is compliant enough to fold without damage, yet robust enough to bear load. In related works, Maleczek et. al. demonstrated a bistable bridge spanning 10 meters constructed out of timber and using thin metal hinge connectors (6). Previous work has also demonstrated textile hinges made of polyester mesh whose flexibility allows folding (7). Large-scale bistable curved-crease columns have also been constructed out of cardboard (8) and polypropylene bubble-core sandwich sheets (9).

To evaluate the feasibility of applying our design method on an architectural scale, we performed a preliminary design and structural analysis for a reconfigurable bench, shown in Fig. 5H and Fig. S16A. The bench surface is initially a cylindrical extrusion of periodic circular arcs with radius of curvature 750 mm. Planar creases were defined, which separate a thin central panel and thick outer panels. During folding, the thin central panel inverts in curvature, while the thick outer panels, which have greater bending rigidity, maintain the same shape and provide a constraint for the edges of the thin central panel. In our design, the thin panel is 1 mm thick and the thick panel is 1.75 mm thick, constructed out of 6061-T6 aluminum, with elastic

modulus of 69 GPa, Poisson's ratio of 0.33, and yield strength of 269 MPa (10). The unfolded bench has a foot print of 2.34 m by 0.70 m, resulting in a total mass of 6.7 kg.

In practice, actuation of the structure could be achieved using hydraulics, pneumatics, ratchet straps, or threaded rods such as in the previously referenced work. In the simulation, first a load of 1000 Newtons was applied to stretch the structure to reduce the bending stiffness. Next, a moment of 69 Nm was applied to both edges of the bench to fold the bench. Then both the stretching load and folding moment were removed, allowing the structure to settle to its second stable state. Next, the feet of the bench were fixed in position, and a downwards body load was applied to the central panel. We found that the structure was able to fold and sustain a load up to 5000 N without any material yielding.

An alternative design shown in Fig. S16B uses the same geometry, but the central panel is the thick shell and the left and right shells are the thin shells. As a result, the central panel maintains the same geometry between the folded and unfolded state, while the outer shells invert in curvature. This design has a mass of 5.8 kg, requires only 23 Nm to fold, and can sustain loads up to 13000 N. The improved performance is likely due to the greatest stresses occurring in the central panel.

Though these designs and simulations are preliminary, they show that our design method is plausible on the architectural scale, and through additional design optimization, such reconfigurable and load-bearing structures may be realizable.

11. Non-planar creases

All of the previously discussed examples including the conical surface shown in Fig. S15 had planar creases, resulting in a binormal vectors $\mathbf{B}(u)$ that were constant to a sign and stable state surfaces which were reflections about the crease plane. Additionally, $\theta_L(u) = \theta_R(u)$, meaning that the ruling angles were identical for both states. For example, if the surface was initially cylindrical with parallel rule lines, the second stable state surface was also cylindrical with parallel rule lines. This is in general not true for non-planar creases.

We solved for the the isometric states of a variety of surfaces with both planar and non-planar creases and plotted the ruled surfaces in Fig. S17 with the expressions of the directrices. Each surface is initially cylindrical with extrusion direction in the $+\hat{z}$ direction. The base curves used for extrusion were circular arcs in Fig. S17A-D, periodic circular arcs that were joined at their ends in Fig. S17E-I, and quartic polynomials in Fig. S17J-K.

If the crease is non-planar, $\tau(u) \neq 0$, the binormal vector is not constant, and in general $\theta_l(u) \neq \theta_R(u)$. As a result, if two stable states exist, the ruling angles will be different. For example, an initially cylindrical shell can snap into a non-cylindrical shell, as shown in the examples in Fig. S17A-C. One can observe that a small modification of the crease shape will result in large changes in the shape of the second stable state. In Fig. S17B, the rule lines diverge, and the resultant surface has a flattened shape. In Fig. S17C, the rule lines converge, resulting in a more conical shape. On the either side of the conical surface, there are no defined rule lines so the shell will take the lowest energy planar surface.

The second stable state may not exist if the calculated isometric surface has intersecting rulings, as shown in Fig. S17D. Additionally, the solution may result in a self-intersecting surface, as in Fig. S17K. Lastly, a second isometric state may not exist even for surface where the ruling lines do not intersect if there is a discontinuity in the ruling direction, as in Fig. S17F. We will discuss this case in more detail.

Suppose the directrix $\mathbf{X}(u)$ and its derivative $\mathbf{X}'(u)$ are continuous, while its second derivative $\mathbf{X}''(u)$ may not be continuous, as in the examples shown in S17E-I, where the normal vector is discontinuous at the interface between circular arcs. The surface found by solving 8 and 9 will be developable with the possible exception at the points at u^* where $\mathbf{X}''(u^*)$ is a discontinuity. At these points, the ruling direction may be discontinuous. Let $\mathbf{R}_L = \mathbf{R}(u^*_-)$ and $\mathbf{R}_R = \mathbf{R}(u^*_+)$. Similarly define φ_L, φ_R, θ_L, θ_R, $\mathbf{N}_L$, $\mathbf{N}_R$, $\mathbf{B}_L$, $\mathbf{B}_R$. Note that $\theta_L \geq \theta_R$, otherwise the ruling lines will intersect. The surface will be non-developable at the discontinuity if the angle between the rule lines on either side of the discontinuity exceeds the difference in the ruling angles in the development, in other words, $\angle(\mathbf{R}_L, \mathbf{R}_R) > \theta_L - \theta_R$. If this is the case, it is impossible to bend a flat triangular patch of angular extent $\theta_L - \theta_R$ to match rule lines with a greater angular distance.

Because $\mathbf{T}$ is continuous, $\mathbf{N}_R$ and $\mathbf{B}_R$ are $\mathbf{N}_L$ and $\mathbf{B}_L$ rotated about the tangent vector. Let

$$\mathbf{N}_R = \cos\gamma \mathbf{N}_L + \sin\gamma \mathbf{B}_L \quad [22]$$

$$\mathbf{B}_R = -\sin\gamma \mathbf{N}_L + \cos\gamma \mathbf{B}_L \quad [23]$$

for a rotation angle γ. Substituting into the expression for the angle between the rule lines with 6,

$$\begin{aligned}
\angle(\mathbf{R}_L, \mathbf{R}_R) &= \arccos(\mathbf{R}_L \cdot \mathbf{R}_R) && [24]\\
&= \arccos((\cos\theta_L \mathbf{T} + \sin\theta_L(\cos\varphi_L \mathbf{B}_L + \sin\varphi_L \mathbf{N}_L)) \cdot (\cos\theta_R \mathbf{T} + \sin\theta_R(\cos\varphi_R \mathbf{B}_R + \sin\varphi_R \mathbf{N}_R))) && [25]\\
&= \arccos(\cos\theta_L\cos\theta_R + \sin\theta_L\sin\theta_R(\cos(\varphi_R - \varphi_L)\cos\gamma + \sin(\varphi_R - \varphi_L)\sin\gamma)) && [26]\\
&= \arccos(\cos\theta_L\cos\theta_R + \sin\theta_L\sin\theta_R\cos(\varphi_R - \varphi_L - \gamma)) && [27]
\end{aligned}$$

Because $0 < \theta(u) < \pi$,

$$\begin{aligned}
\angle(\mathbf{R}_L, \mathbf{R}_R) &= \arccos(\cos\theta_L\cos\theta_R + \sin\theta_L\sin\theta_R\cos(\varphi_R - \varphi_L + \gamma)) && [28]\\
&\geq \arccos(\cos\theta_L\cos\theta_R + \sin\theta_L\sin\theta_R) && [29]\\
&\geq \arccos(\cos(\theta_L - \theta_R)) && [30]
\end{aligned}$$

Therefore,

$$\varphi_R - \varphi_L - \gamma = 2\pi N, \qquad N \in \mathbb{Z} \tag{31}$$

is necessary for the surface to developable at the discontinuity. Furthermore, if we consider the first isometric state, with inclination angles $-\varphi_L$ and $-\varphi_R$ and a continuous surface normal vector $\mathbf{P}(u)$, from 4 and substituting 22 and 23

$$\begin{aligned}
\cos\varphi_L\mathbf{B}_L - \sin\varphi_L\mathbf{N}_L &= \cos\varphi_R\mathbf{B}_R - \sin\varphi_R\mathbf{N}_R && [32]\\
&= \cos\varphi_R(-\sin\gamma\mathbf{N}_L + \cos\gamma\mathbf{B}_L) - \sin\varphi_R(\cos\gamma\mathbf{N}_L + \sin\gamma\mathbf{B}_L) && [33]\\
&= (\cos\varphi_R\cos\gamma - \sin\varphi_R\sin\gamma)\mathbf{B}_L - (\cos\varphi_R\sin\gamma + \sin\varphi_R\cos\gamma)\mathbf{N}_L && [34]\\
&= \cos(\varphi_R+\gamma)\mathbf{B}_L - \sin(\varphi_R+\gamma)\mathbf{N}_L && [35]\\
&\Rightarrow \varphi_L - \varphi_R - \gamma = 2\pi M, \qquad M \in \mathbb{Z} && [36]
\end{aligned}$$

Combining 31 and 36, we find

$$\begin{aligned}
\gamma &= -\pi(N+M) && [37]\\
\varphi_R - \varphi_L &= \pi(N-M), \qquad N, M \in \mathbb{Z}, && [38]
\end{aligned}$$

meaning the surface is developable only if the Frenet frame is continuous or rotated by π radians about the tangent vector at the discontinuity. Note for planar creases where the binormal vector is constant up to a sign, this is automatically satisfied.

The normal vector can be expressed as

$$\mathbf{N}(u) = \frac{\mathbf{X}'(u)\times(\mathbf{X}''(u)\times\mathbf{X}'(u))}{|\mathbf{X}'(u)\times(\mathbf{X}''(u)\times\mathbf{X}'(u))|}. \tag{39}$$

The surface will be developable only if $\mathbf{X}''(u^*_-) \parallel \mathbf{X}''(u^*_+)$.

For instance, in Fig. S17F, the surface with crease $z(u) = y(u) + 0.002y(u)^2$ has no second isometric state, because a gap exists at the discontinuity. This can be verified by calculating the second derivative of the position vector at $u^* = s_0$.

$$\mathbf{X}''(u^* = s_{0-}) = (-\frac{1}{R}\sin(\frac{s_0}{R}), -\frac{1}{R}\cos(\frac{s_0}{R}), -\frac{1}{R}\cos(\frac{s_0}{R}) + 2a\sin^2(\frac{s_0}{R})) \tag{40}$$

$$\mathbf{X}''(u^* = s_{0+}) = (\frac{1}{R}\sin(\frac{s_0}{R}), \frac{1}{R}\cos(\frac{s_0}{R}), \frac{1}{R}\cos(\frac{s_0}{R}) + 2a\sin^2(\frac{s_0}{R})) \tag{41}$$

It is clear that the $y(u)^2$ term prevents the normal vectors on either side of the discontinuity from being parallel. In contrast, in Fig. S17G with crease $z(u) = y(u) + 0.002y(u)^2(-1)^{\lfloor\frac{t+s_0}{2s_0}\rfloor}$ is developable because the $y(u)^2$ is negated at the interface. Similarly, the surface shown in Fig. S17H with an $y(u)^3$ term has two isometric states, because the second derivative of $y(u)^3$ is 0 at the interface. The surface in Fig. S17I has semi-circular arcs, resulting in $x'(u) = 0$ at the interfaces. As a result, two isometric states exist even with a $x(u)^2$ term in the $z(u)$ function.

To validate the geometric modeling for non-planar creases, a comparison between the analytical and numerical solutions of samples with $R = 55$, $s_0 = 45$, and $z = y$, $z = y - 0.005y^2$, and $z = y + 0.005y^2$ (similar to Fig. S17A-C) are shown in Fig. S18A. A small variation in the crease curve results in shells that can be flatter or more conical than the cylindrical solution. The numerical solution was found by modeling a thin surface with thickness of 0.05 mm in order to reduce the bending stiffness. Starting with the initial cylindrical surface, a horizontal body force was applied to the shell in order to fold the crease. Then the body force was removed to allow the shell to settle to the second stable state. The shape of the second stable state from the analytical and numerical solutions have good agreement except at the left and right edges of the shell, which is potentially due to the bending stiffness and initial curvature of the cylindrical shell, which are not considered in the analytical solution. In addition, we only analyzed a single set of geometries, and changing parameters such as the length of the cylinder may affect the discrepancy between analytical and numerical solutions. Note that in Fig. S18A the conical sample's peak energy density is greater than that of the other two samples because surface curvature increases when approaching the apex of a cone.

In Fig. S18B we show physical prototypes constructed out of PET sheets using the same non-planar creases, where the green shells maintain the original cylindrical surface, while the red shells correspond to the folded configurations. We can observe the variations in shell geometry that result from changes in crease geometry, which match the trends from the analytical and numerical solutions. Differences between the numerical solution and the shape of the physical prototypes could be due to the shell being initially cylindrical in the numerical solution, while the sheet is initially flat in the physical prototypes. In addition, the stiffness in the creases of the physical prototypes may influence the folded shapes, which is not modeled in the numerical solution.

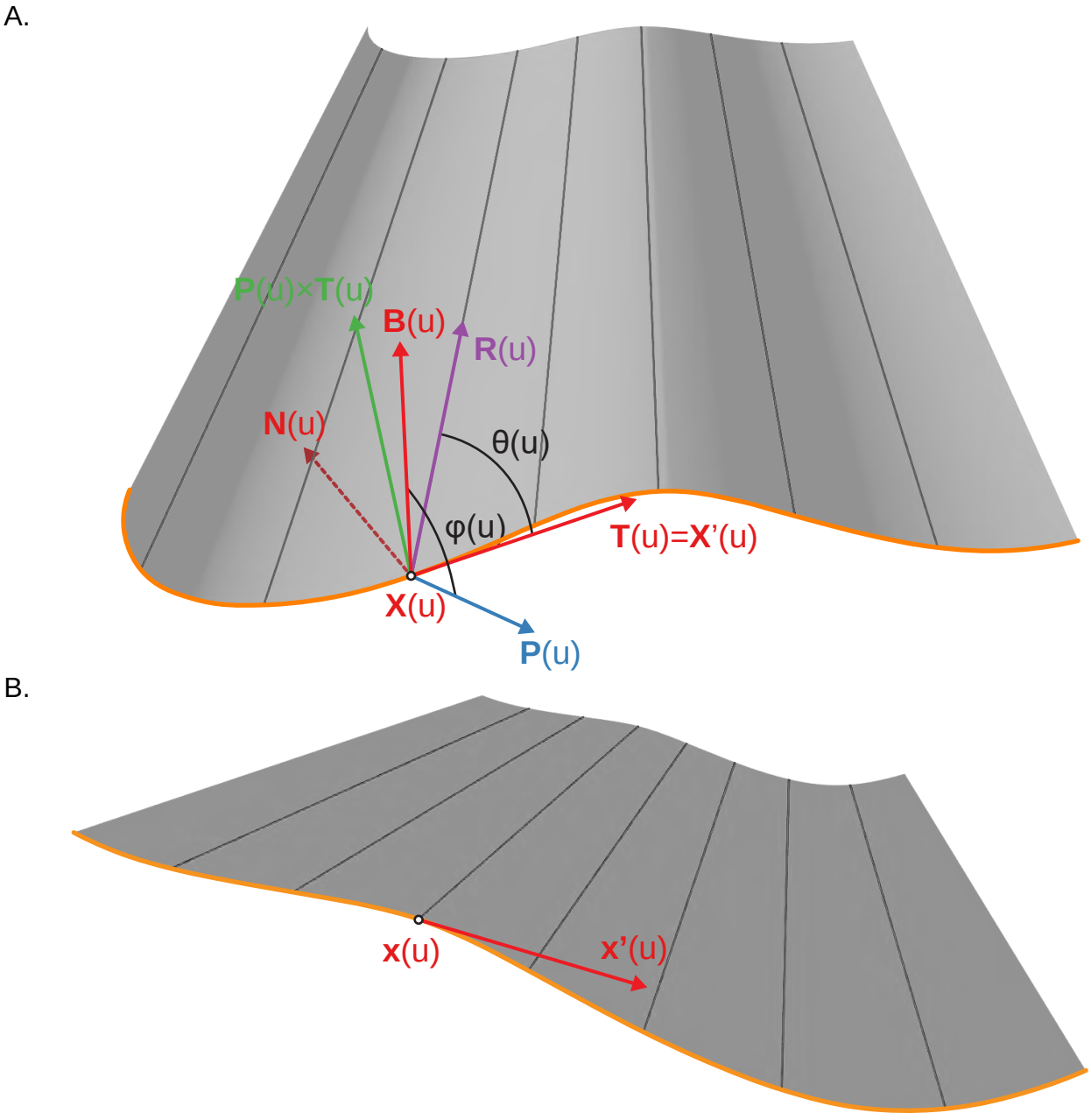

Fig. S1. (A) A ruled surface defined by directrix $\mathbf{X}(u)$ and ruling directions $\mathbf{R}(u)$. The Frenet-Serret frame $(\mathbf{T}(u), \mathbf{N}(u), \mathbf{B}(u))$ is shown in red. Additionally, $\mathbf{P}(u)$ is the normal direction of the surface at $\mathbf{X}(u)$. The inclination angle $\varphi(u)$ and ruling angle $\theta(u)$ are also shown. (B) The development of the ruled surface is shown with boundary curve $\mathbf{x}(u)$.

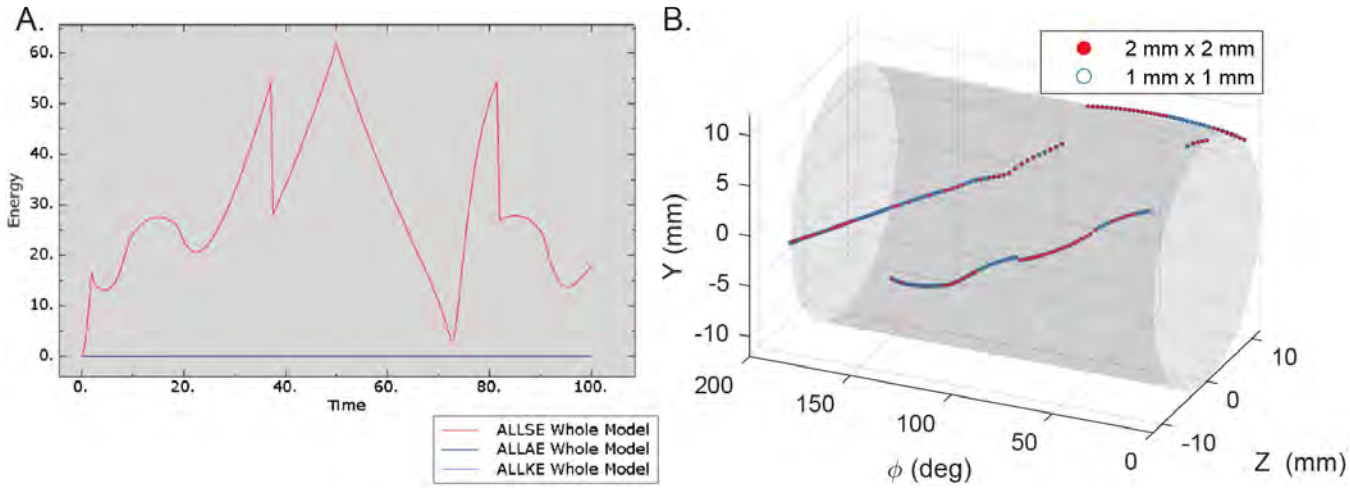

Fig. S2. FEM verification for baseline sample: (A) Total strain energy, artificial energy, and kinetic energy plotted against simulation time. (B) Branch diagram for 2 mm x 2 mm mesh and 1 mm x 1 mm.

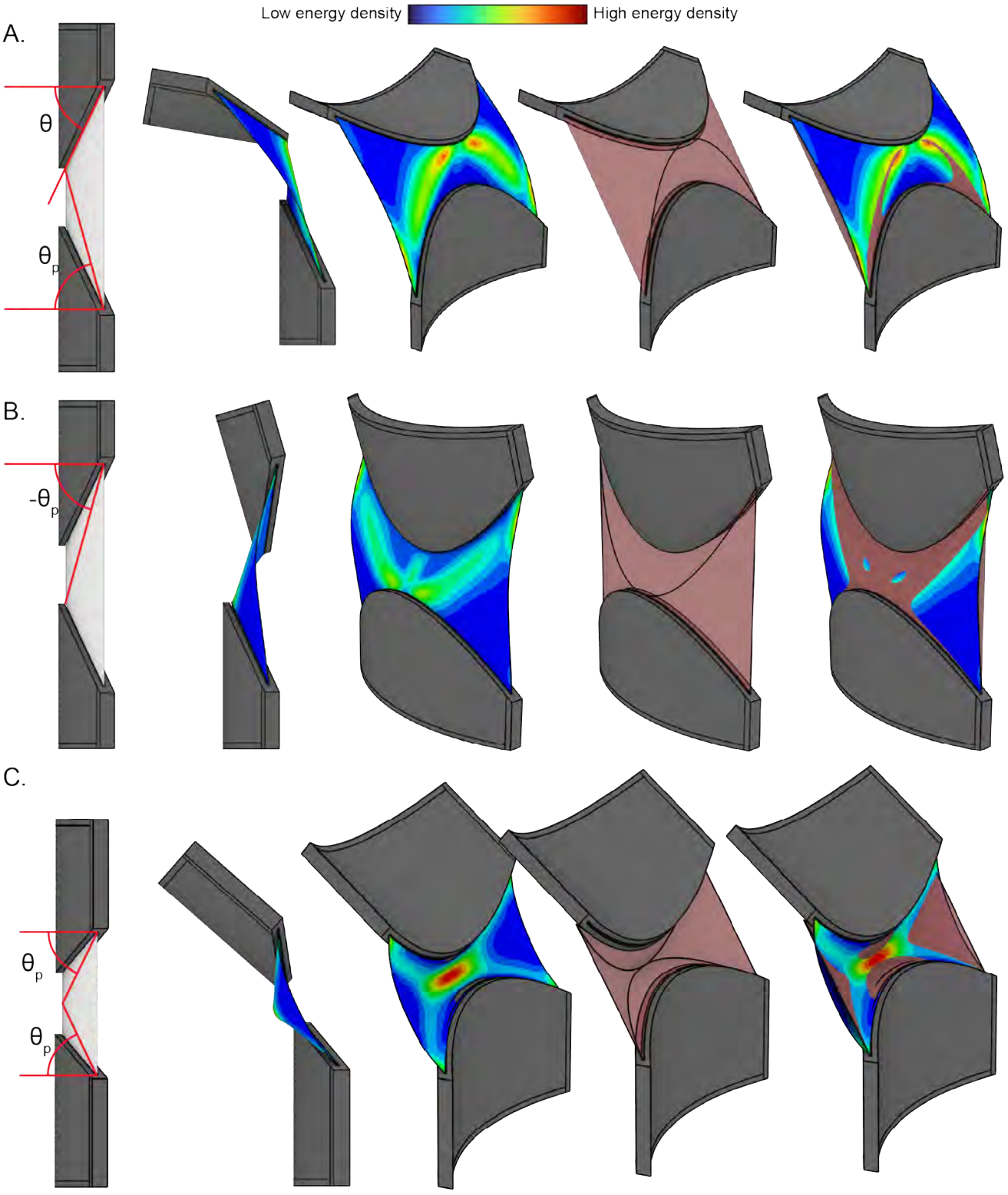

Fig. S3. Comparison between simulated stable states and shape predicted by approximating sharp planar pseudo-creases and applying reflections. On the left, the angles between the horizontal plane and the (psuedo-)crease planes are shown. The simulated shapes colored by strain energy density are displayed along with the predicted shape in red. The rightmost figures show the overlay of the two shapes. (A) and (B) show States C and B respectively of the sample shown in Fig. 2 and the first sample in Fig. S4. (C) shows State F of the second sample in Fig. S4 with two pseudo-creases.

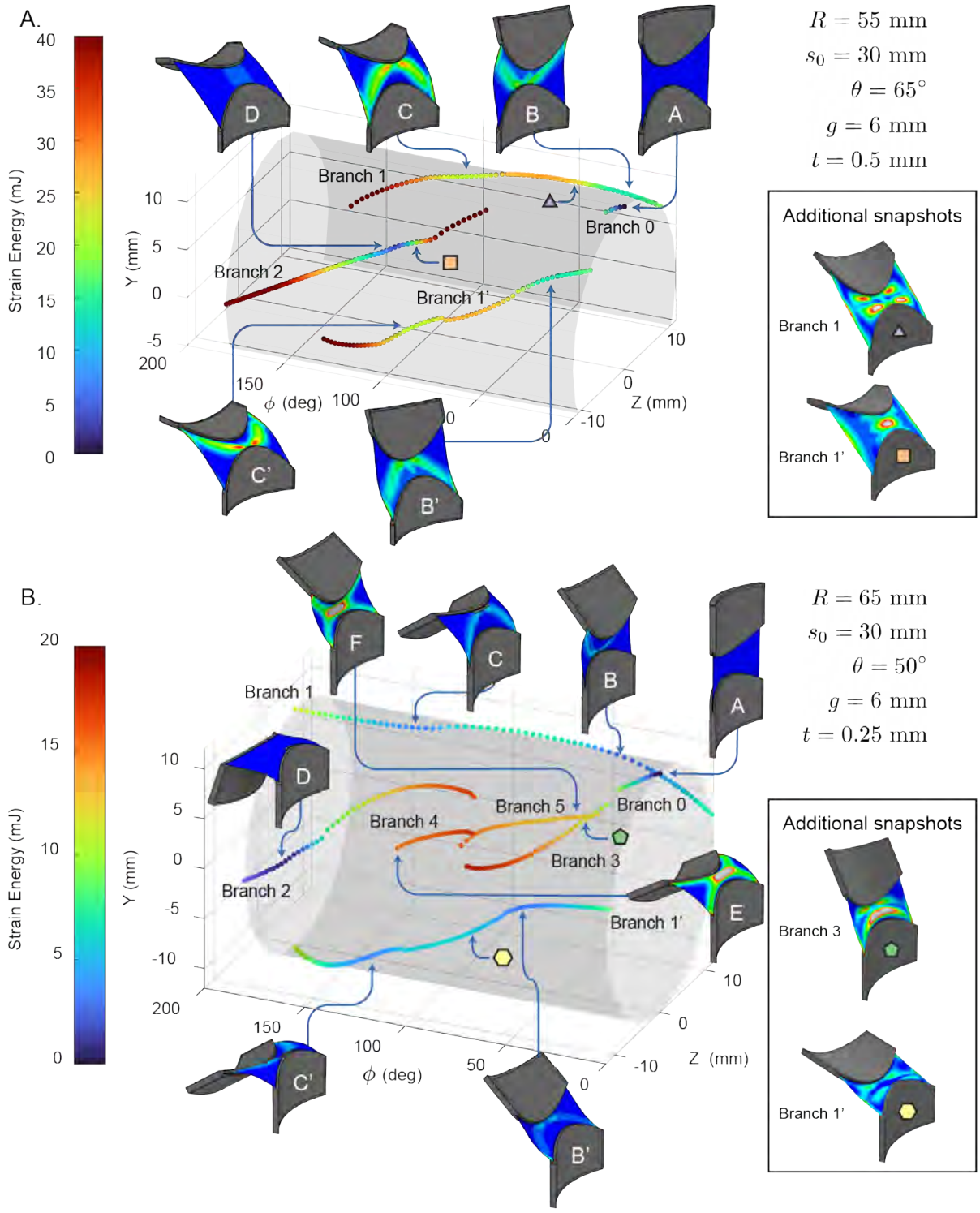

Fig. S4. Branch diagrams for (A) ($R = 55$ mm, $s_0 = 30$ mm, $\theta = 65^\circ$, $g = 6$ mm, $t = 0.5$ mm) and (B) ($R = 65$ mm, $s_0 = 30$ mm, $\theta = 50^\circ$, $g = 6$ mm, $t = 0.25$ mm). The stable states found in the simulation are shown. Additional snapshots between states of local minima energy are also shown.

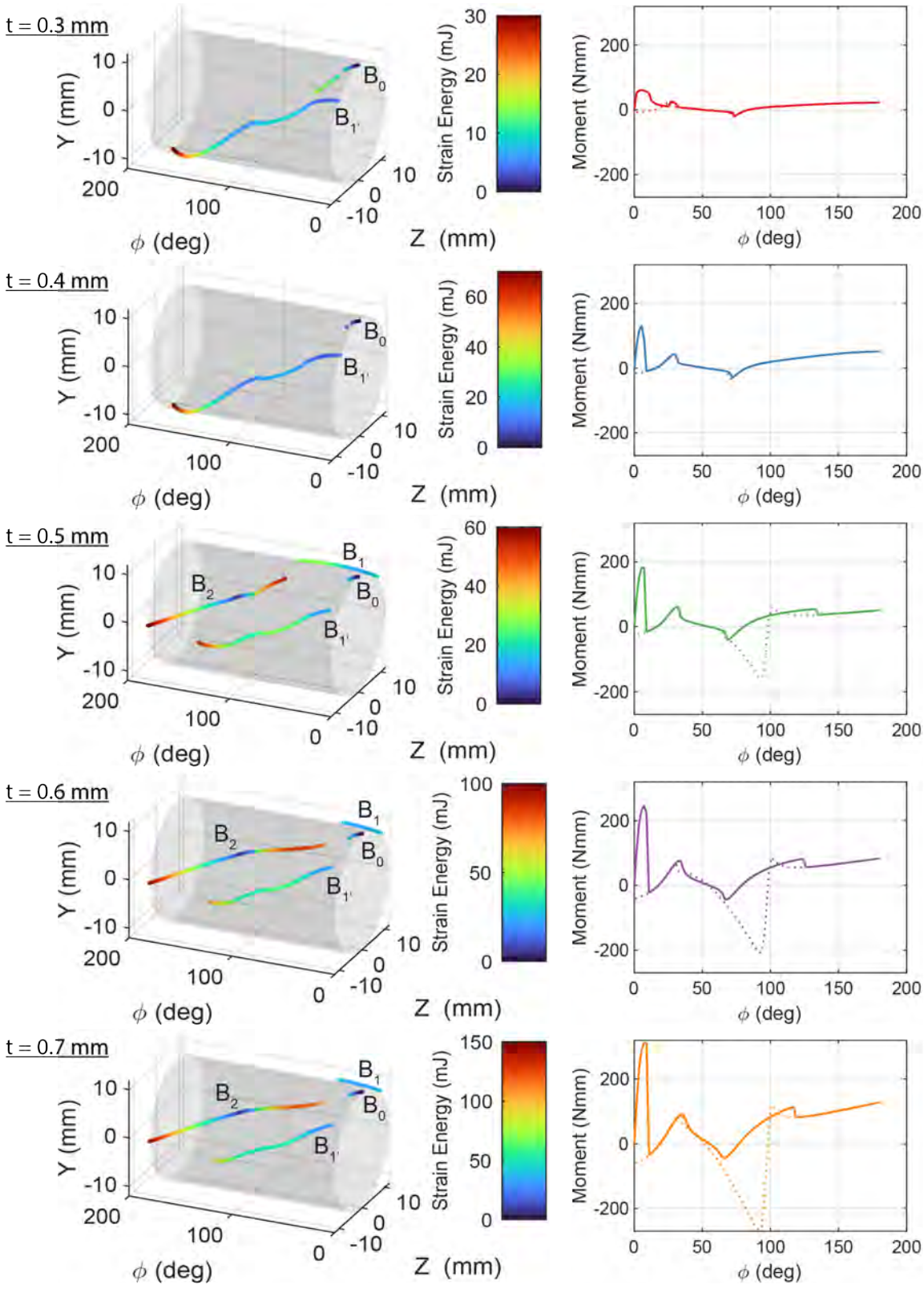

Fig. S5. Branch diagrams and moment vs. ϕ plots for rotation sweeps for various shell thicknesses with $(R = 55\,\text{mm}, s_0 = 30\,\text{mm}, \theta = 65^\circ, g = 6\,\text{mm})$ and $t = \{0.3\,\text{mm}, 0.4\,\text{mm}, 0.5\,\text{mm}, 0.6\,\text{mm}, 0.7\,\text{mm}\}$

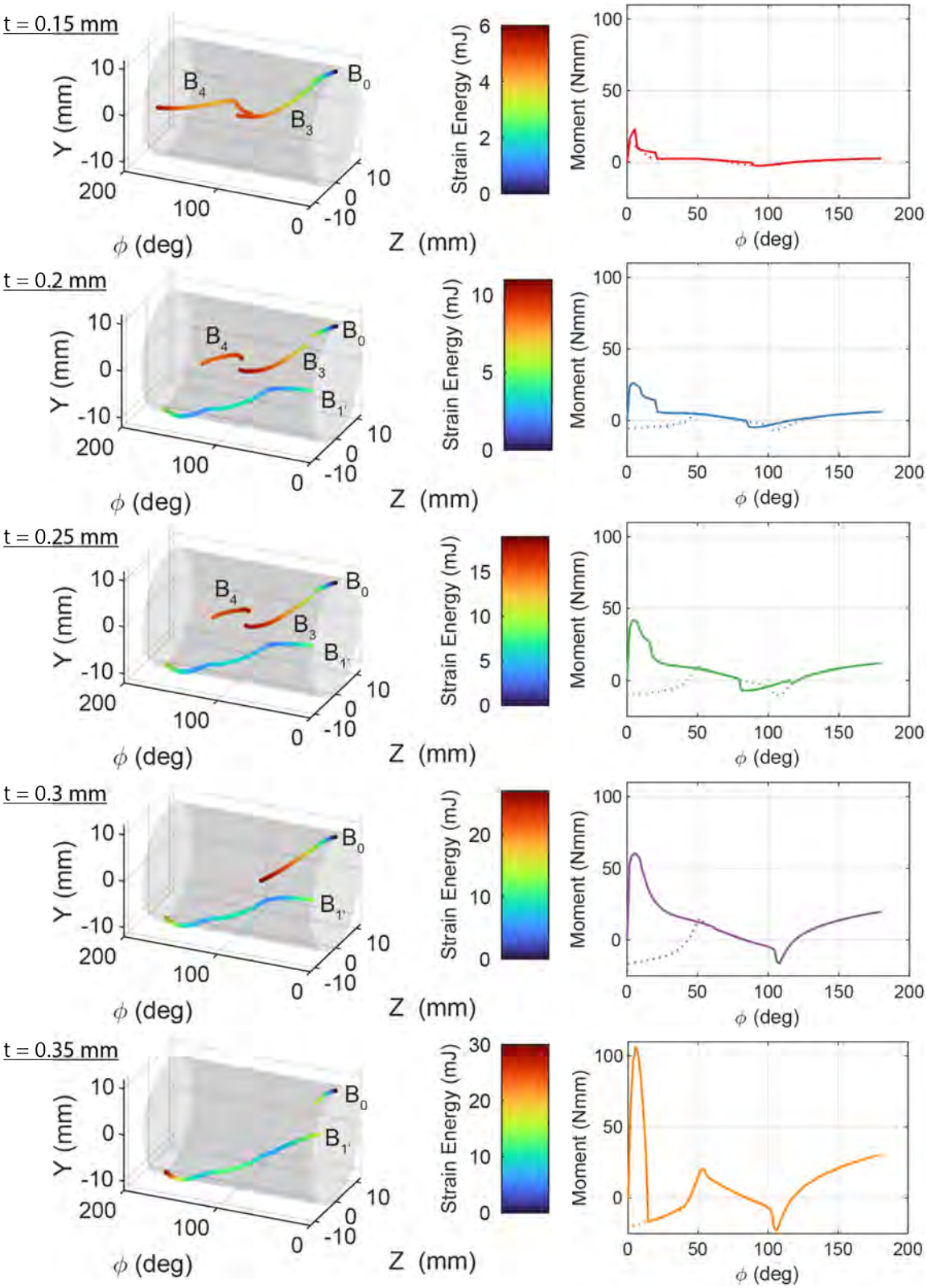

Fig. S6. Branch diagrams and moment vs. ϕ plots for rotation sweeps for various shell thicknesses with $(R = 65\text{ mm}, s_0 = 30\text{ mm}, \theta = 50^\circ, g = 6\text{ mm})$ and $t = \{0.15\text{ mm}, 0.2\text{ mm}, 0.25\text{ mm}, 0.3\text{ mm}, 0.35\text{ mm}\}$

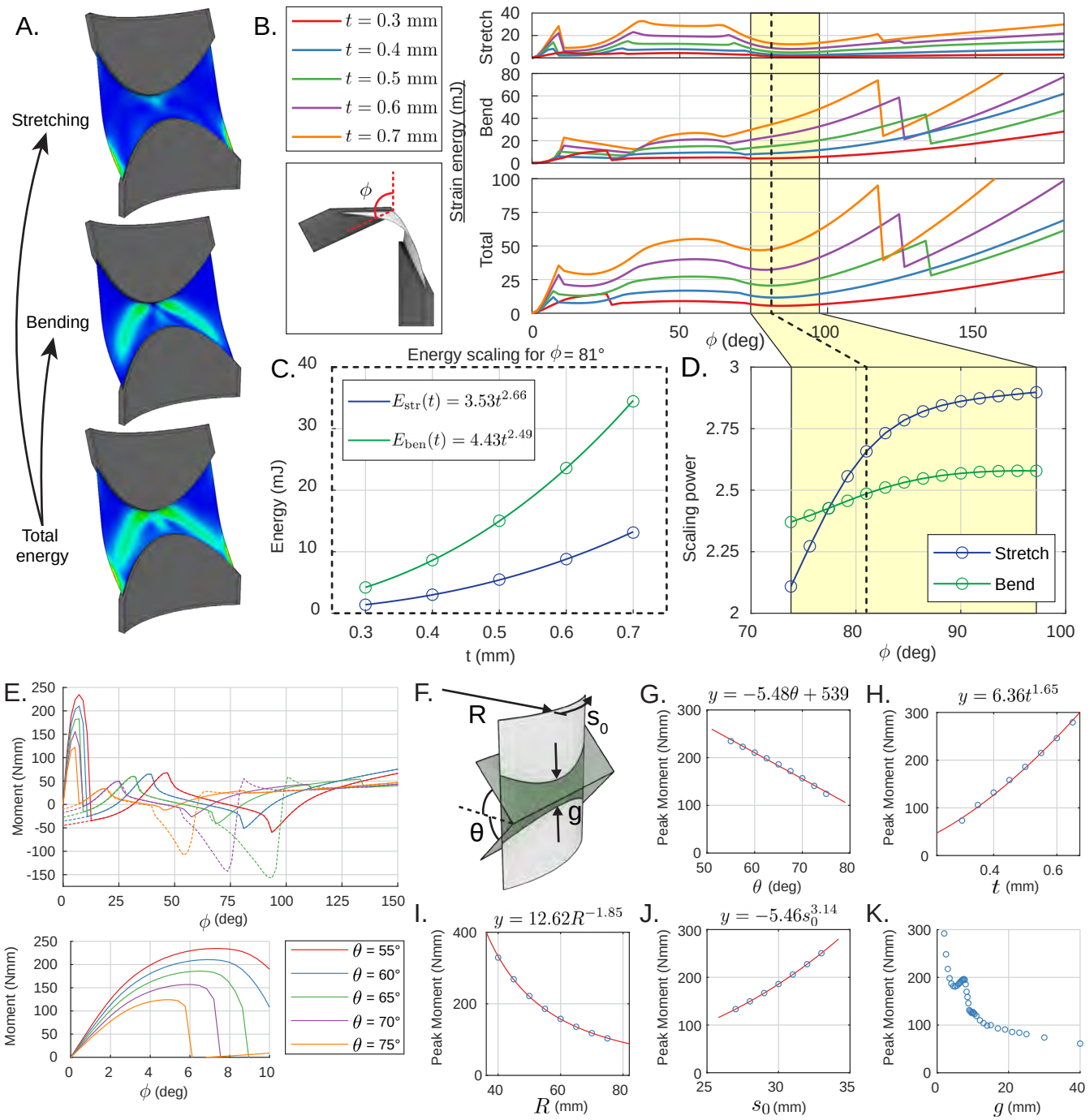

Fig. S7. Quantitative simulation results. (A-D) focus on the decomposition of the straining energy into stretching and bending energies, and show the scaling with thickness for a sample with ($R = 55$ mm, $s_0 = 30$ mm, $\theta = 65°$, $g = 6$ mm). (A) Decomposition of strain energy density into stretching and bending components for the stable state of $\phi = 18°$ for $t = 0.5$ mm. (B) Strain energies vs. handle rotation angle for a variety of shell thicknesses. (C) Scaling of stretching and bending energies as a function of thickness for $\phi = 81°$. (D) Variation of scaling power for the range of $74° < \phi < 97°$, in which all simulated thicknesses are on the same branch. (E-K) show the effect of varying geometric parameters. (E) Moment vs. rotation plots for a variety of inclination plane angles θ values. Solid lines represent the loading direction and dotted lines represent the unloading direction. The sharp jumps in moment that can be observed occur when the shell snaps between different branches, as depicted in Fig. **??**. Different branches in the forward and backward direction also explain the hysteresis shown in the samples with $\theta \geq 65°$. The bottom plot highlights the initial portion of the moment vs. rotation plot. (F) Diagram illustrating geometric parameters. (G-K) Plots of peak moment vs. various geometric parameters. A linear function was fit for θ and power law functions were fit for t, R, and s_0.

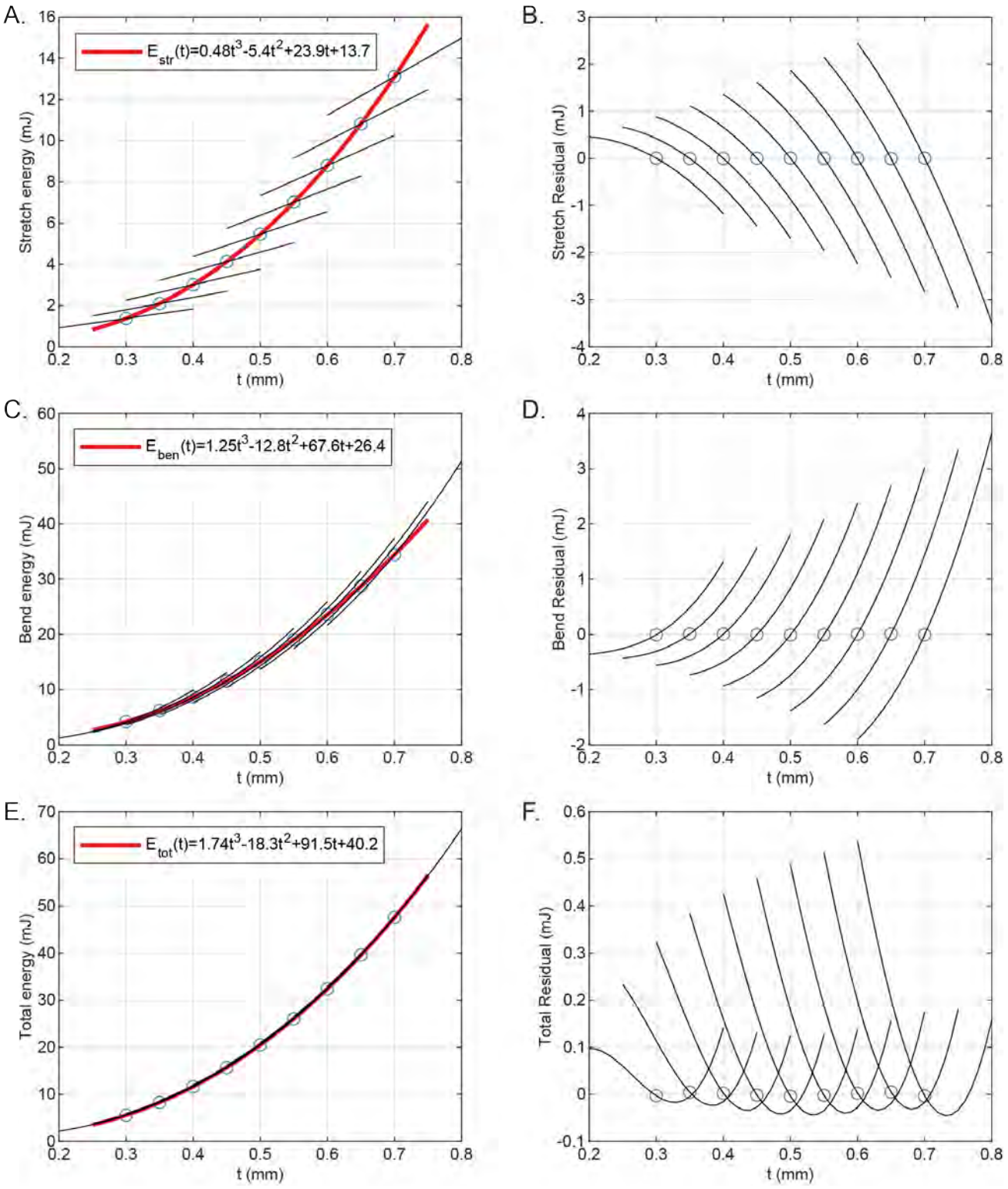

Fig. S8. Energy scaling with thickness. (A) Simulated stretching energy data points fitted to a cubic polynomial. For each data point, a short segment is plotted which corresponds to a linear relationship between stretching energy and thickness. (B) Residuals when the polynomial fit is subtracted from the data points. One can observe the stretching energy increases faster than linearly. (C) Simulated bending energy data points fitted to a cubic polynomial. For each data point, a short section is plotted which corresponds to a cubic relationship between stretching energy and thickness. (D) Residuals when the polynomial fit is subtracted from the data points. One can observe the bending energy increases slower than cubically. (E) Total energy data points fitted to a cubic polynomial. For each data point, a short section is plotted which corresponds to the sum of the linear and cubic scalings of stretching energy and thickness. (F) Residuals when the polynomial fit is subtracted from the data points. One can observe from (E) and (F) that the summed scaling is close to tangent to the simulated energy, with the simulated total energy close to the minimum of the scaled and summed energy.

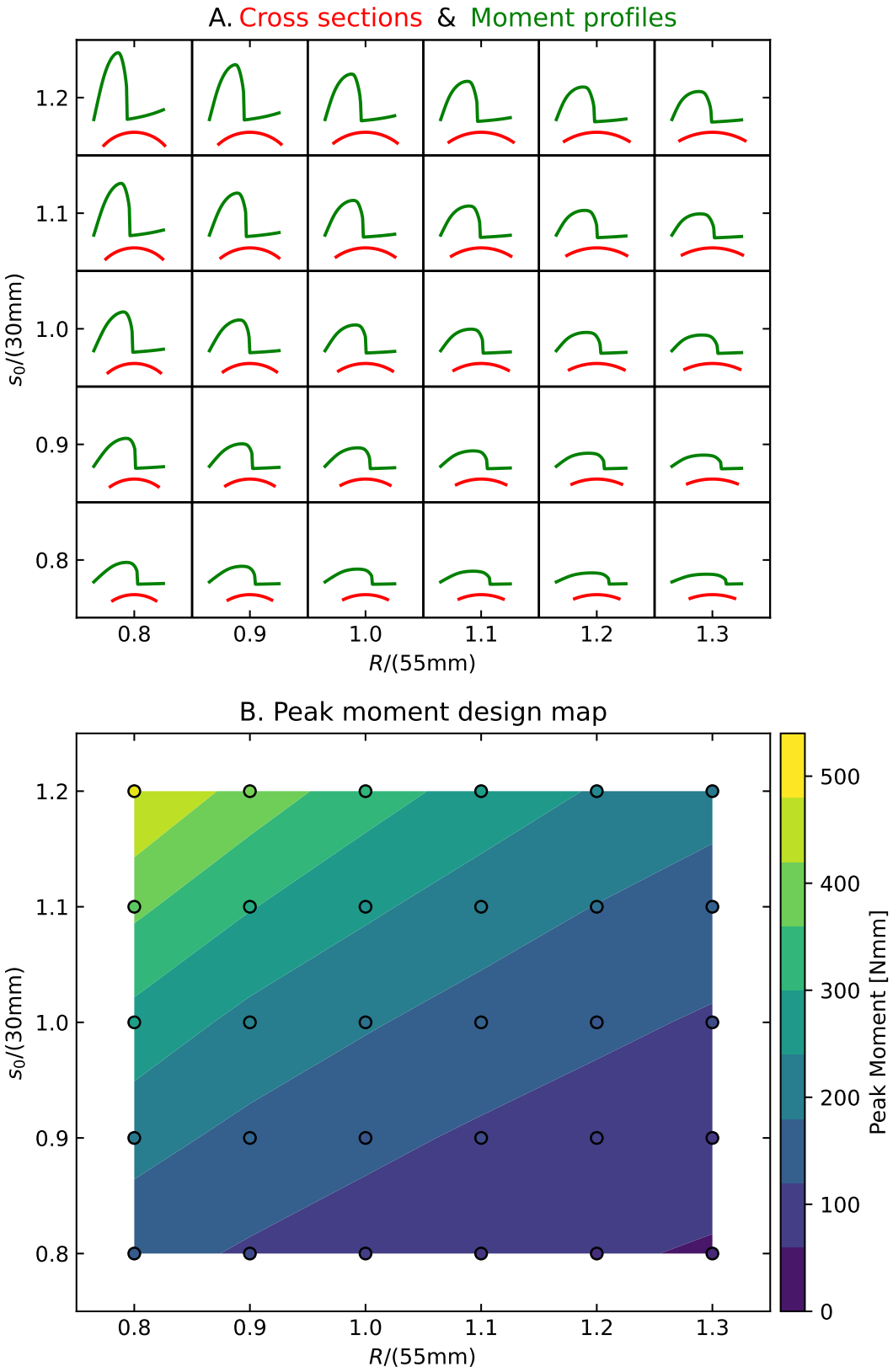

Fig. S9. Design map for peak moment varying radius of curvature R and semi-arc length s_0. Simulations were conducted varying R and s_0 simultaneously, for a total of 30 simulations. (A) For each simulation, a sketch of the sample cross section is shown in red and a sketch of the moment versus rotation angle is shown in green (rotation angle ranges from 0° to 15°). (B) Peak moment contour map interpolating the simulation results from (A).

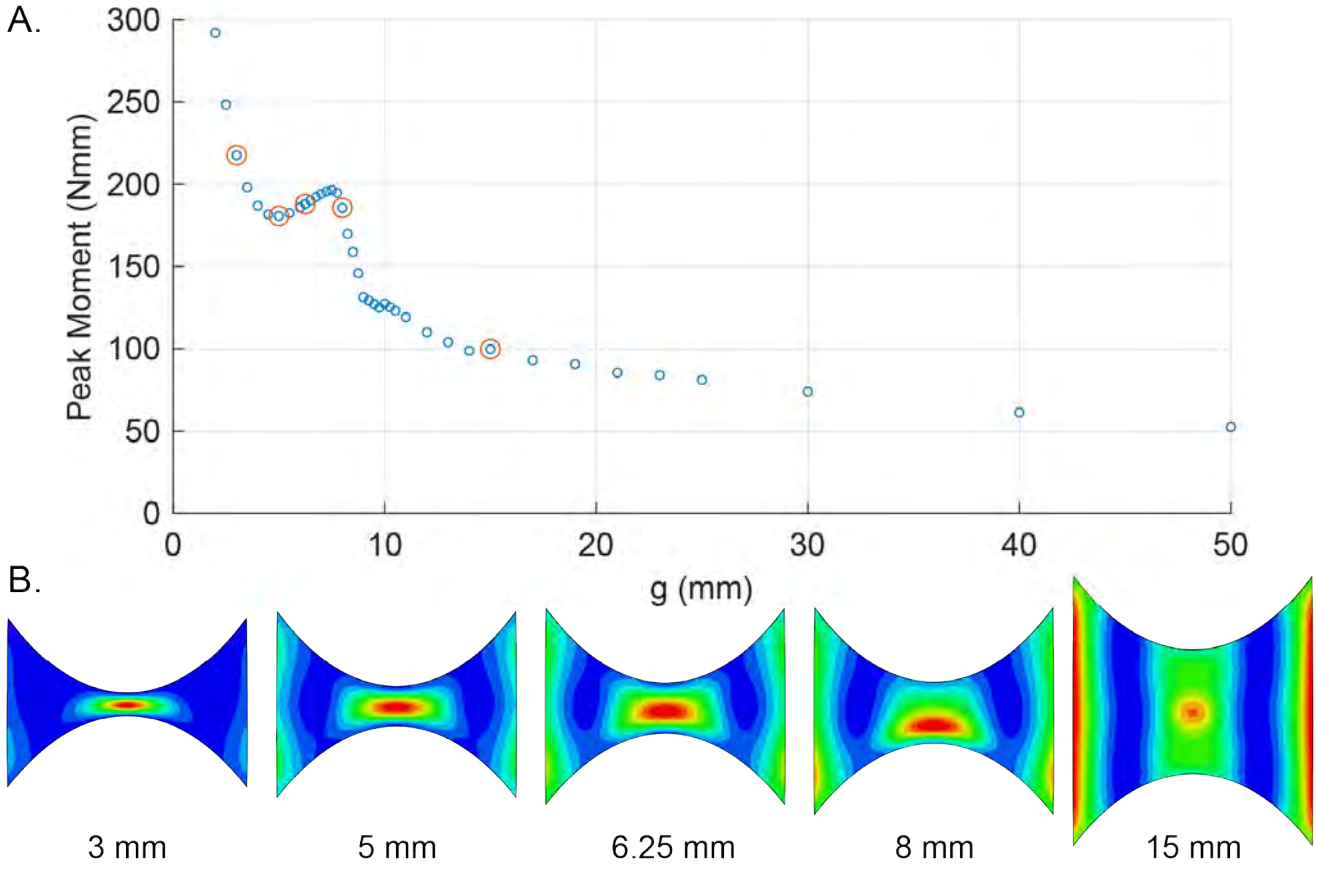

Fig. S10. Relationship between peak moment and gap length. (A) Peak moment vs. gap length plot. (B) Snapshots of the shells colored by energy density when they exert their peak moment for the five thickness highlighted in red in (C). Based on the strain energy distribution, we theorize a mechanistic explanation for the relationship between the peak moment and gap length. At very low values of g, there is little material at the center of the sample to compress, causing the neutral axis to shift inwards and the second moment of inertia to increase. For intermediate values of g, such as $g = 5$ mm, 6.25 mm, and 8mm, the deformation is localized near one crease, resulting in a relatively weak relationship between peak moment and g. For large values of g, the deformation is localized in the center of the shell, resembling a tape spring in bending, so the peak moment approaches a constant value.

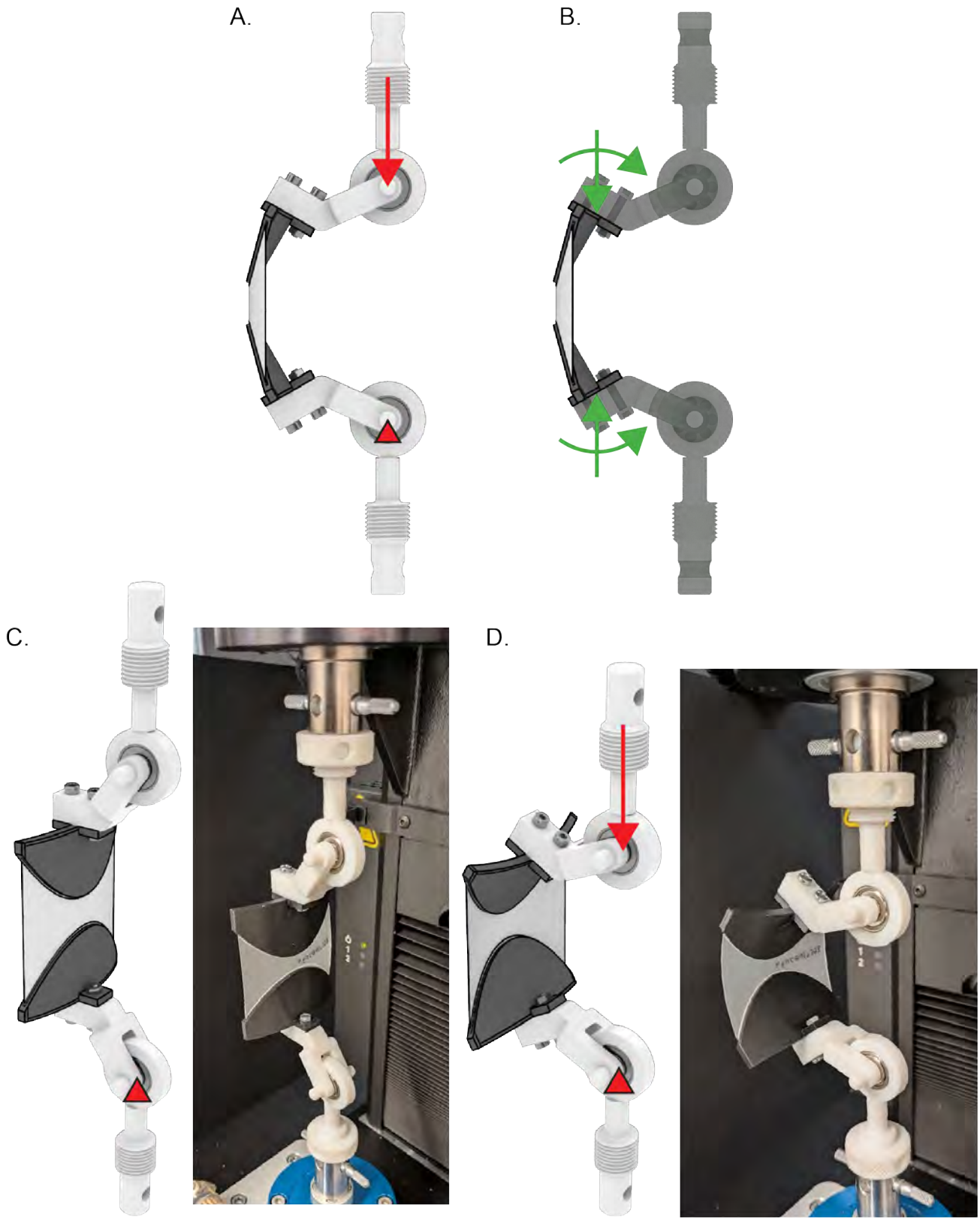

Fig. S11. Instron test setup (A) Side view of test fixture attached to snapping sample, with displacement control and boundary conditions indicated. (B) Side view with force and moment reactions on sample indicated. (C-D) Comparison between CAD models and physical test setup.

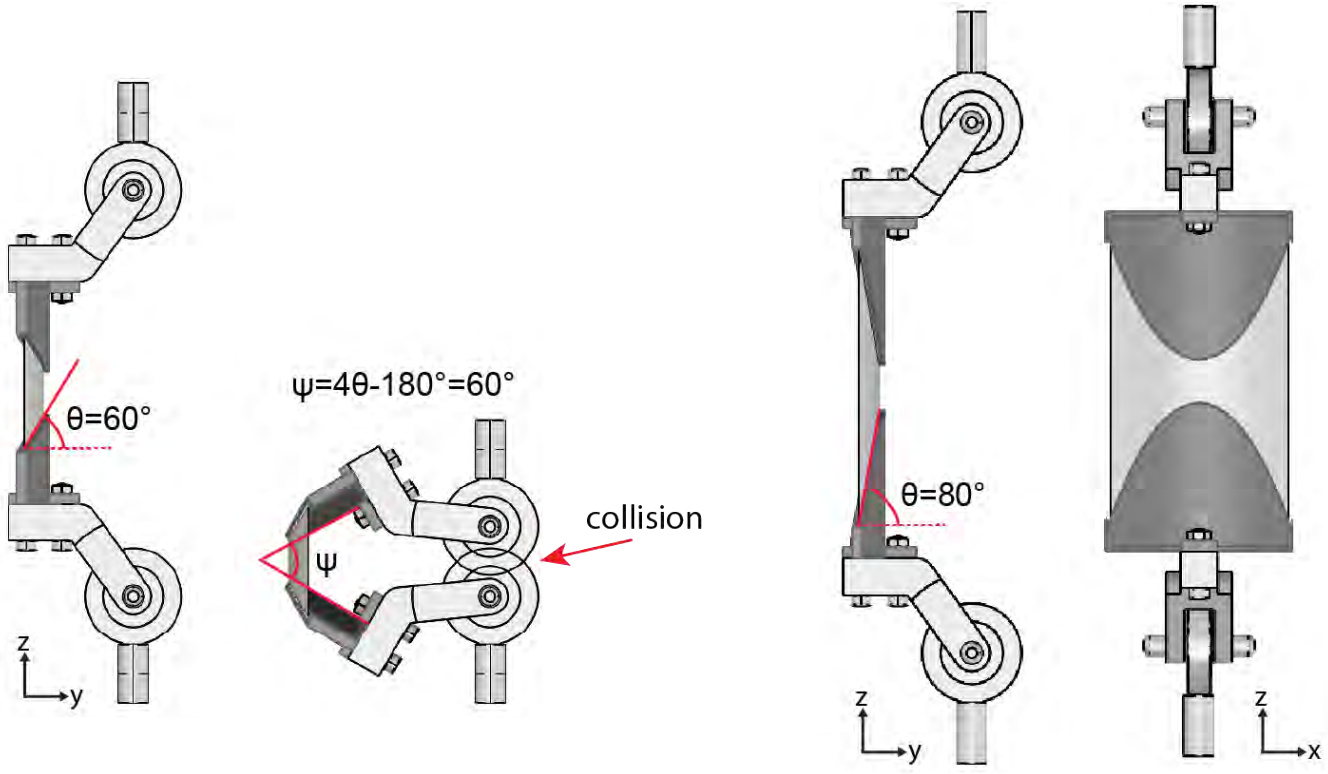

Fig. S12. Examples of test samples with (A) low θ value which results in collision during testing, and (B) large θ value which results in extremely long creases.

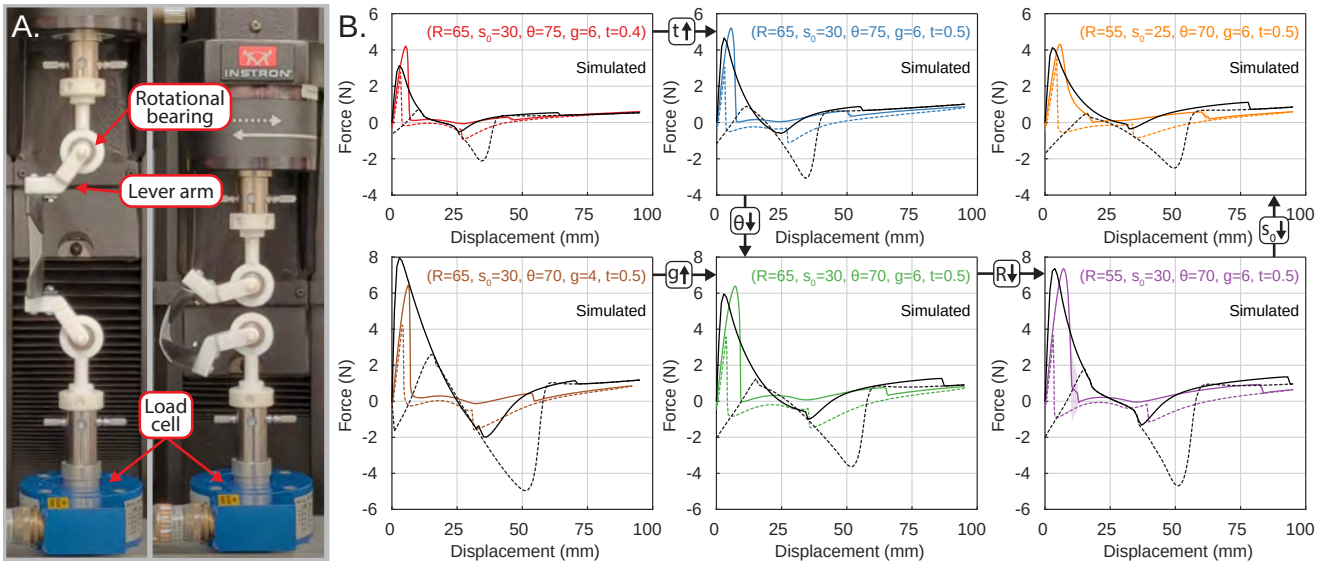

Fig. S13. (A) Test setup (B) Load vs displacement plots for 6 samples with different geometric parameters (R, s_0, θ, g, t). Length measurements are given in mm and angle measurements are given in degrees. Arrows between adjacent plots indicate where only one geometric parameter is different. The solid lines represent the loading portion, while the dotted lines represents the unloading portion, when the tester head moves upwards. The majority of trends predicted in simulations are validated in the experiments. One can observe the following trends: increased thickness results in higher stiffness, decreased θ results in higher equilibrium fold angle and higher peak load, lower g results in earlier snapping, lower R and higher s_0 result in higher peak load. We do not see a significantly higher peak load for the sample with lower g, however this is not so surprising based on the complex relationship between g and peak load and the simplifying assumptions made in the numerical model.

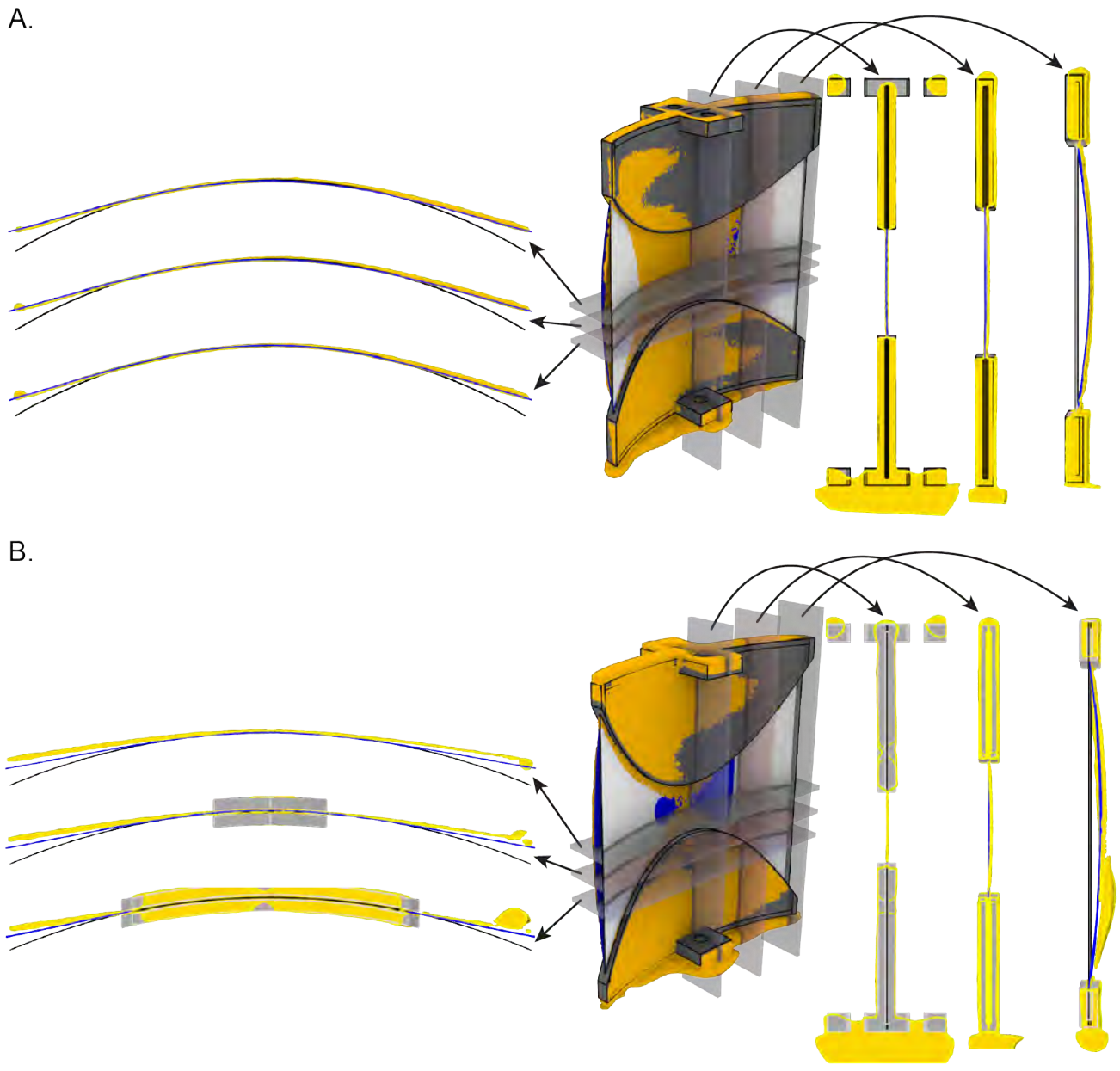

Fig. S14. Overlay comparisons between idealized cylindrical shell, simulated shapes from bending an initially flat sheet and 3D scans of physical models using an Einscan-SP tabletop scanner. Idealized cylindrical surfaces are gray, the simulated shape from bending a flat sheet is shown in blue, and the scanned shape is shown in orange. We also show 1 mm thick cross sections slices. (A) Sample with $(R = 55\,\text{mm}, s_0 = 30\,\text{mm}, \theta = 60^\circ, g = 9\,\text{mm}, t = 0.5\,\text{mm})$. (B) Sample with $(R = 75\,\text{mm}, s_0 = 30\,\text{mm}, \theta = 75^\circ, g = 6\,\text{mm}, t = 0.5\,\text{mm})$. We see good agreement between the simulation and scan for the sample with $R = 55$ mm, however the simulation underestimates the flattening effect for the sample with $R = 75$ mm.

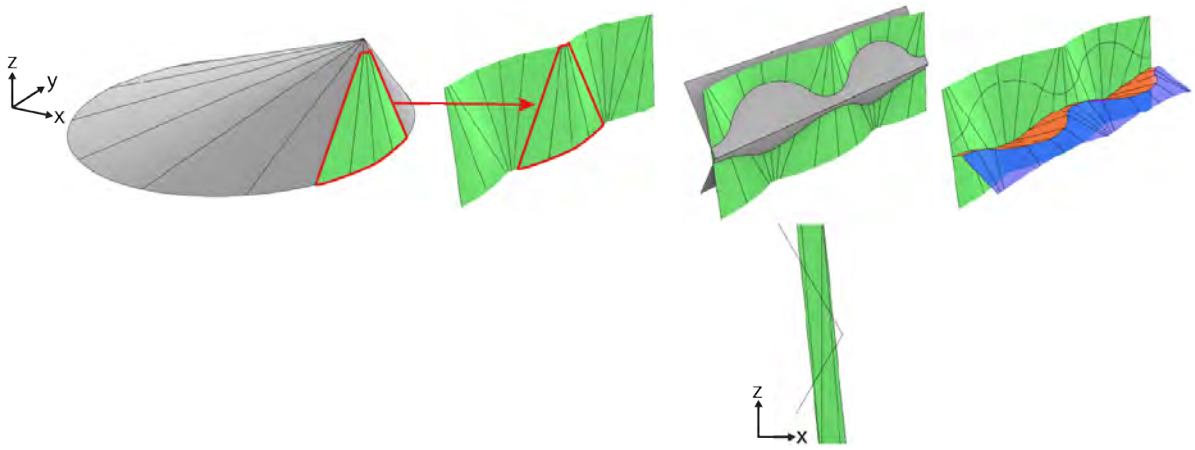

Fig. S15. Graphical description of the geometry of the conical surfaces shown in Fig. 5B found by joining sections of a cone and defining creases by intersecting with planes.

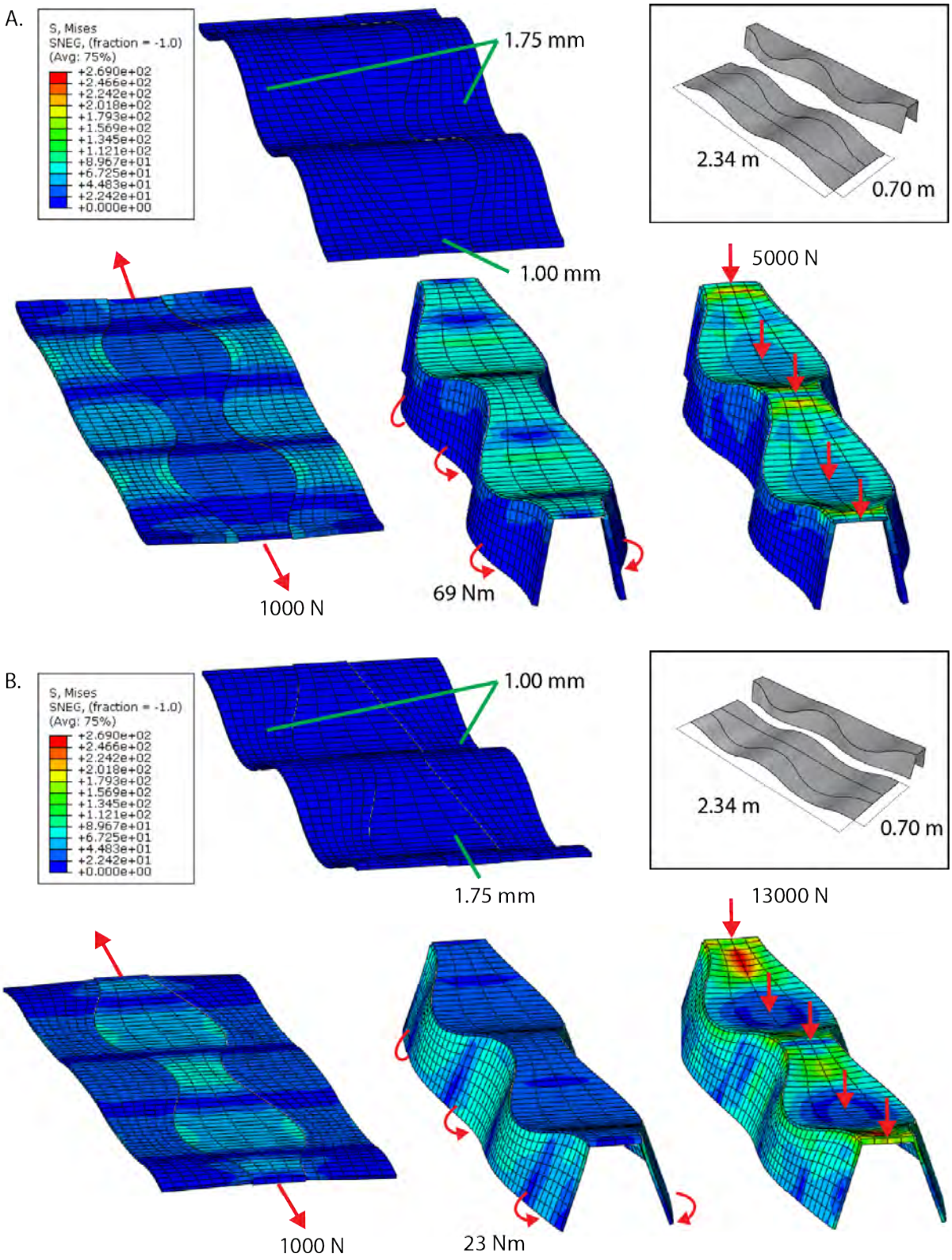

Fig. S16. Two preliminary designs and analyses of the conceptual bench shown in Fig. 5H. For each design, snapshots of a finite element simulation are shown colored by von Mises stress in units of MPa. The simulation sequence for both designs consists of first applying a stretching load of 1000 N, applying a bending moment to fold the bench, releasing both loads, fixing the bench feet, and applying a vertical body load until failure. The design in (A) has a thin central panel and thick outer panels, while the design in (B) has a thick central panel and thin outer panels. In the folding process, the thin panels invert in curvature. The thicknesses of the panel in the simulations are scaled by a factor of 10 for visibility.

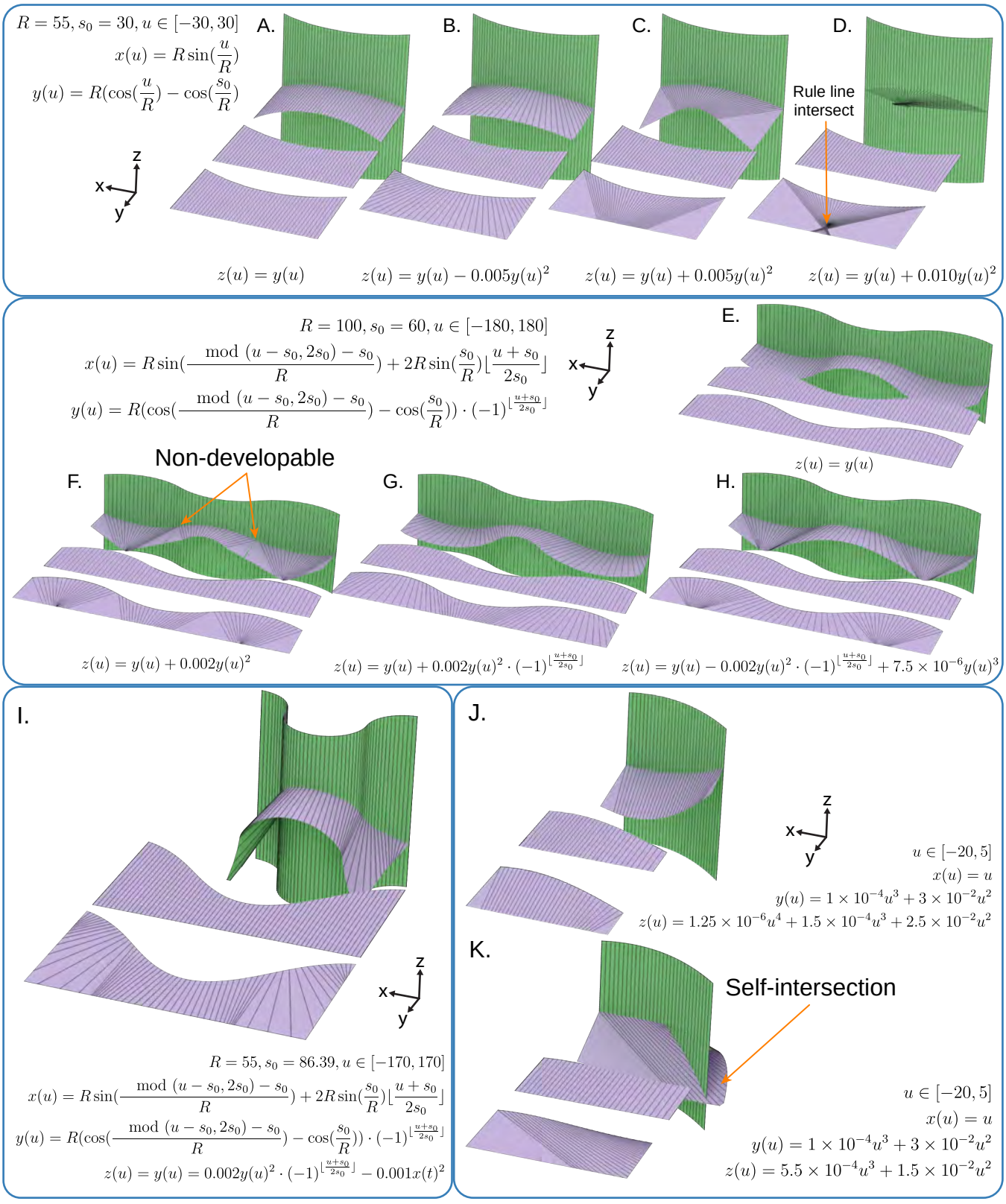

Fig. S17. Samples with planar and non-planar creases showing ruling lines and developments. All samples are initially cylindrical extrusions of a base curve. The base curves are circular arcs for A-D, periodic circular arcs joined at ends for E-I and quartic polynomial curves for J-K. Making creases non-planar can change the rule lines in the second stable state from parallel (A) to diverging (B) or converging (C). If rule lines intersect, as in (D), the second isometric state does not exist. The diretrices in (E-H) have discontinuous second derivatives, which can cause non-developable points at the discontinuity, as in (F). Appropriately choosing the expression of the directrix will allow the second isometric state, as in (G) and (H). (I) use semi-circular arcs, which causes $x'(u) = 0$ at the discontinuity, which allows a $x(u)^2$ while maintaining developability. The second isometric state also may not exist due to self-intersection of the surface, as in (K).

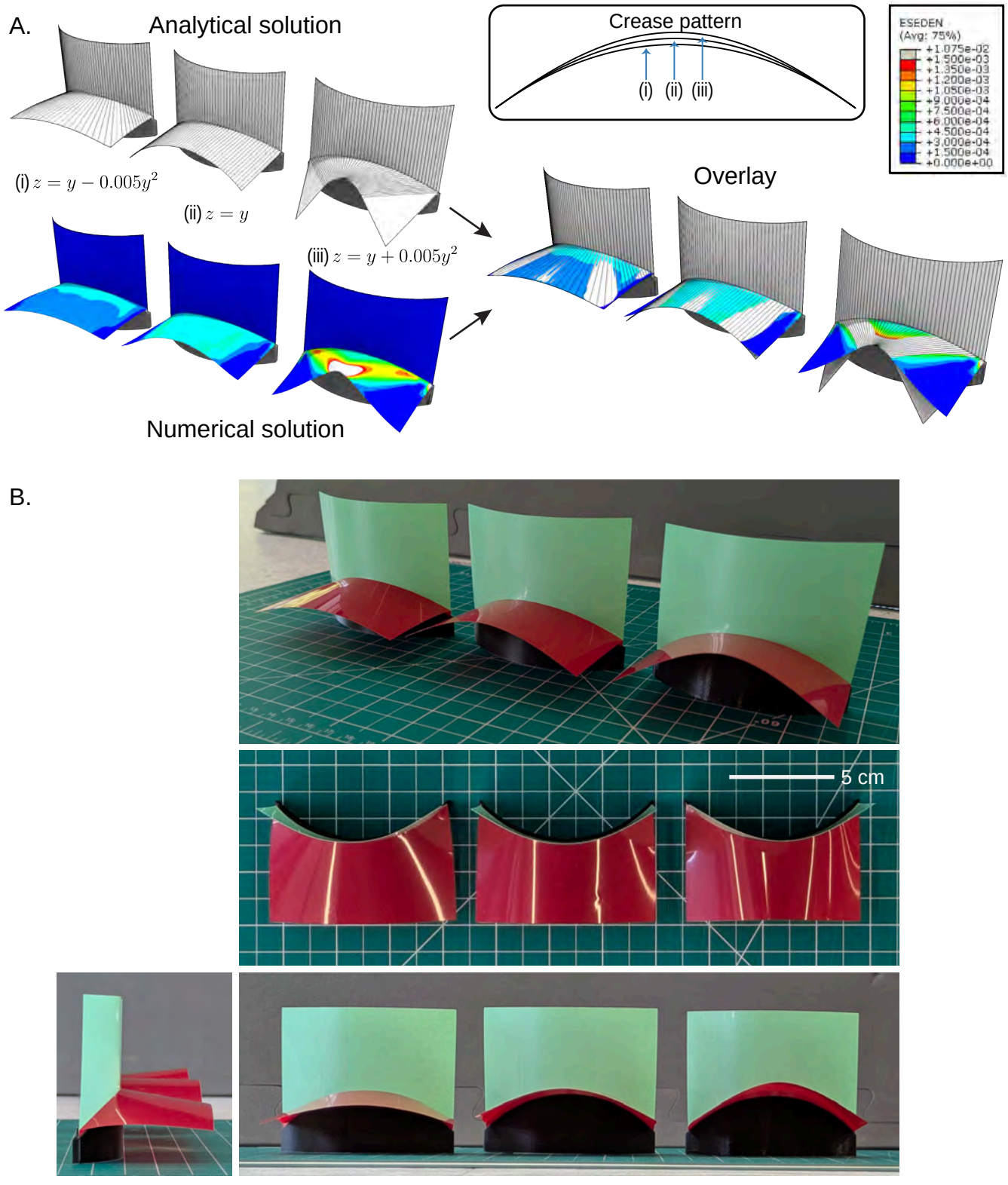

Fig. S18. Simulations and prototypes with cylindrical cross sections $(R = 55, s_0 = 45)$ with planar or non-planar creases (i) $z = y - 0.005y^2$, (ii) $z = y$, and (iii) $z = y + 0.005y^2$. (A) Comparison between analytical and numerical solutions. The ruling lines are shown on the analytical solution, and the simulated solution is colored by strain energy density in units of $\frac{\text{mJ}}{\text{mm}^2}$. An overlay of the two solutions is shown for comparison. In addition, the crease patterns of the three curves in the flat development are shown in the inset. (B) Physical prototypes of the samples analyzed in (A) are shown in multiple perspectives, which demonstrate qualitatively the influence of the crease geometry on the stable configuration geometry. The green sheet represents the initial cylindrical shell, and the red sheet represents the folded configuration.

Movie S1. Magnetic actuation of a curved-crease robot.

Movie S2. Physical and numerical models of snapping origami.

Movie S3. Thickness variation's impact on stretching and bending energy.

Movie S4. Simulation and experimental validation.

Movie S5. Generalizations and applications.

SI Dataset S1 (angleSweep.py)
Python script to run ABAQUS simulations of angular sweeps.

SI Dataset S2 (instronTest.py)
Python script to run ABAQUS simulations replicating experimental setup.

SI Dataset S3 (nonPlanarCrease.gh)
Grasshopper script to solve for isometric states of non-planar creases.

References

1. K Mundilova, Ph.D. thesis (Massachusetts Institute of Technology) (2024).
2. Polypropylene Properties (https://www.vinidex.com.au/resources/technical-resources/material-properties/polypropylene-properties/) (2025) [Online; accessed 20-May-2025].
3. CR Calladine, *Theory of shell structures*. (Cambridge university press), (1983).
4. A Lobkovsky, S Gentges, H Li, D Morse, TA Witten, Scaling properties of stretching ridges in a crumpled elastic sheet. *Science* **270**, 1482–1485 (1995).
5. EinScan-SP V2 (https://www.einscan.com/einscan-sp/) (2025) [Online; accessed 23-May-2025].
6. R Maleczek, M Bernhard, R Maderebner, C Preisinger, Fold and snap-flatpacking a wooden beam in *Proceedings of IASS Annual Symposia*. (International Association for Shell and Spatial Structures (IASS)), Vol. 2024, pp. 1–9 (2024).
7. R Maleczek, G Stern, A Metzler, C Preisinger, Large scale curved folding mechanisms in *Design Modelling Symposium Berlin*. (Springer), pp. 539–553 (2019).
8. M Lee, M Abu-Saleem, T Tachi, JM Gattas, A lightweight building construction system using curved-crease origami blocks in *International Meeting on Origami in Science, Mathematics and Education*. (Springer), pp. 253–264 (2024).
9. M Lee, JM Gattas, T Tachi, Multistable curved-crease origami blocks for reconfigurable modular building system. *arXiv preprint arXiv:2509.07337* (2025).
10. Aluminum 6061-t6; 6061-t651 material data sheet (https://asm.matweb.com/search/specificmaterial.asp?bassnum=ma6061t6) (n.d.).